Synthesis of a Novel Diblock Copolymer and Preparation of Highly Selective Molecularly Imprinted Polymer Nanospheres from It

By

Bolu Peng

A thesis submitted to the Department of Chemistry

In conformity with the requirement for the

degree of Master of Applied Science

Queen's University

Kingston, Ontario, Canada

(August, 2015)

Abstract

Crosslinking monomers or a polymer around template molecules and the subsequent removal of the templates yield a polymer matrix containing cavities that resemble the shape of the templates and bear binding groups that complement those on the template molecules. However, a key challenge facing those molecularly imprinted polymers (MIPs) is the infidelity of the pores generated to the original templates and thus non-specific binding of the pores to analytes other than the template. I report in this thesis a method to improve the selectivity of MIP particles.

I prepared an MIP for a chiral analyte relying not only on the traditional H-bonding interactions between the polymer matrix and the template but also on the π-π stacking interactions. Specifically, I synthesized a novel diblock copolymer poly(ethylene oxide)$_{226}$-*block*-poly[(2-pentafluorocinnamoyloxyethyl methacrylate)$_{75\%}$-*ran*-[2-(2'-carboxybenzoyloxy)ethyl methacrylate]$_{25\%}$]$_{100}$ or PEO$_{226}$-*b*-P(FEMA$_{75\%}$-*r*-CA$_{25\%}$)$_{100}$. While the CA groups were introduced because of their H-bond interactions with carbonyl oxygen and amino group of the chiral template *D*-phenylalanine anilide, the FEMA units were introduced for their ability to crosslink under the UV irradiation and also for the π-π stacking interactions of the fluorinated FEMA phenyl rings with the phenyl rings of *D*-phenylalanine anilide. To prepare MIP nanoparticles, I first dispersed the diblock copolymer and *D*-phenylalanine anilide in chloroform/methanol at 95 vol% of methanol to prepare micelles that bore PEO coronal chains and a P(FEMA-*r*-CA) core that complexed with *D*-phenylalanine anilide. I then photocrosslinked the micellar core and locked the

FEMA and CA units around the template molecules. In a third step, I extracted out *D*-phenylalanine anilide using a solvent. I discovered that these crosslinked MIP nanoparticles had a selectivity of 6.3 towards the binding of *D*-phenylalanine anilide over *L*-phenylalanine anilide. This represented a 70% increase in selectivity of MIP nanoparticles prepared from an analogous approach by replacing PEO_{226}-*b*-P($FEMA_{75\%}$-*r*-$CA_{25\%}$)$_{100}$ with PEO_{226}-*b*-P($CEMA_{75\%}$-*r*-$CA_{25\%}$)$_{100}$, where CEMA is the hydrogenated version of FEMA. I believe that my work pinpoints the opportunity for using π-π stacking interactions between fluorinated and hydrogenated aromatic rings for improving the selectivity of MIPs and the potential of using this interaction in future for developing highly selective MIPs.

Acknowledgements

First, and most importantly, I extremely appreciate my supervisor Prof. Guojun Liu for accepting me as a member of this caring, mutually helping and creative research group. Under his supervision, I've learned and gained a lot knowledge and experience from research work. Every time when I met difficulties and felt frustrated, Dr. Liu would be generous to offer help. Therefore, I am so grateful to his guidance and encouragement along this way.

I also would like to thank all of my committee members, Prof Philip G. Jessop and Prof Simon A.M. Hesp for passing on their valuable ideas and knowledge to me.

Many thanks to all of the past and present members in Liu's group. I am grateful to Dr. John Dupont. Without his generous help, the research work would be way more difficult for me in the early stage. I would like to thank Dr. Heng Hu for passing his experience in polymer synthesis on me. I would also like to thank our technician, Jian Wang for her assistance with AFM analysis. I am also appreciate Dr. Ian Wyman for his great assistance with my thesis writing. My special thanks also go to all of the other members: Yu Wang, Dr. Ganwei Zhang, Weijie Jiang, Zijie Wang, Kaka Zhang, Shuaishuai Huang, Dr. Wu Xu, Dr. Muhammad Rabnawaz and Dr. Claudia Grozea for the friendship and help in the past two years.

Last but not the least, I want to give my deepest appreciation to my parents in China for their unconditional love, mentally and financially support and encouragement. Without you, I can barely pursue my goals and nothing will be possible for me. To you I owe a profound and lifetime debt.

Thank all the people who helped me along this way!

Table of Contents

List of Figures

List of Tables

List of Abbreviations

AFM – Atomic Force Microscopy

ATRP – Atom Transfer Radical Polymerization

DCM – Dichloromethane

DLS – Dynamic Light Scattering

$_D$-ΦAA – D-phenylalanine anilide

FEMA – 2-pentafluorocinnamoyloxyethyl methacrylate

HEMA – 2-hydroxyethyl methacrylate

HEMA-TMS – 2-[(trimethylsilyl)oxy]ethyl methacrylate

$_L$-ΦAA – L-phenylalanine anilide

MIT – Molecular Imprinting Technology

PEO-OH - Poly(ethylene glycol) methyl ether

PCEMA – Poly(cinnamoyl 2-oxyethyl methacrylate)

PHEMA – Poly(2-hydroxyethyl methacrylate)

PFEMA – Poly(2-pentafluorocinnamoyloxyethyl methacrylate)

PFOEMA – Poly[2-(perfluorooctyl)ethyl methacrylate]

SEC – Size Exclusion Chromatography

SEM – Scanning Electron Microscope

Chapter 1

Introduction

1.1 Research Objective and Organization of Thesis

Crosslinking monomers or a polymer around dispersed template molecules and the subsequent removal of the templates yield a polymer matrix containing cavities that resemble the shape of the templates and possess binding groups that complement those on the template molecules. This molecular imprinting technology (MIT) first developed in 1972 by Wulff et al. is now widely used for various applications, such as organic separation, chromatography, drug delivery, and various other areas. Most of the research work reported before was focused on monomers or polymers featuring one or two types of noncovalent interactions between host polymer and the imprinted templates. Here, we introduce a third type of noncovalent interaction to the binding system to enhance the selectivity of molecularly imprinted polymer (MIP) particles.

The goal of this thesis was to design and synthesize a novel block copolymer poly(ethylene oxide)-*block*-poly[(2-pentafluorocinnamoyloxyethyl methacrylate)-*ran*-[2-(2'-carboxybenzoyloxy)ethyl methacrylate]] (PEO-*b*-P(FEMA-*r*-CA)) and to develop a facile method to prepare imprinted polymer nanospheres with high selectivity. We firstly synthesized the macroinitiator PEO-Br and then reacted it with 2-[(trimethylsilyl)oxy]ethyl

methacrylate (HEMA-TMS) via atom transfer radical polymerization. The block copolymer poly(ethylene oxide)$_{226}$-*block*-poly(2-hydroxyethyl methacrylate)$_{100}$ (PEO$_{226}$-*b*-PHEMA$_{100}$, with repeating unit 226 and 100, respectively) was subsequently successively chemically modified with pentafluorocinnamic acid chloride and phthalic anhydride to yield poly(ethylene oxide)$_{226}$-*block*-poly[(2-pentafluorocinnamoyloxyethyl methacrylate)$_{75\%}$-*ran*-[2-(2'-carboxybenzoyloxy)ethyl methacrylate]$_{25\%}$]$_{100}$, (PEO$_{226}$-*b*-P(FEMA$_{75\%}$-*r*-CA$_{25\%}$)$_{100}$,with 75% and 25% of HEMA repeating unit reacted with pentafluorocinnamic acid chloride and phthalic anhydride, respectively). See Figure 1-1. The PEO$_{226}$-*b*-P(FEMA$_{75\%}$-*r*-CA$_{25\%}$)$_{100}$ block copolymer mixed with D-phenylalanine anilide ($_D$-ΦAA) was made as a micellar solution in a chloroform/methanol mixture at *v*/*v* = 0.5/9.5 and irradiated under UV to photocrosslink the FEMA double bond and achieve a 70% double bond conversion. See Figure 1-2, 1-3. The $_D$-ΦAA was then removed by dialysis against methanol/chloroform at *v*/*v* = 2/8. The polymer nanospheres were then collected by precipitation in diethyl ether.

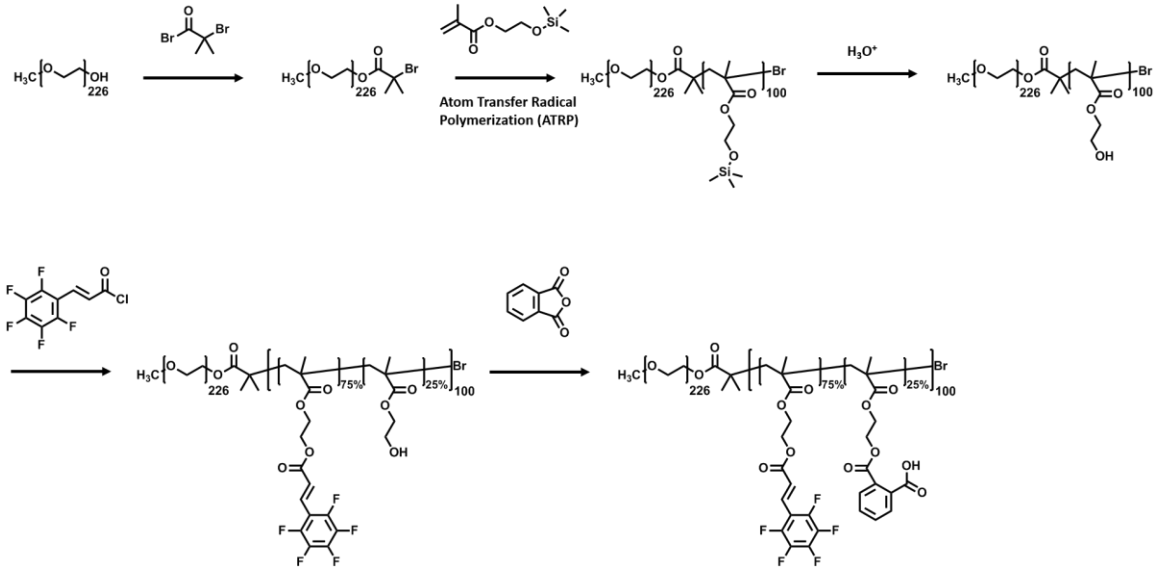

Figure 1-1. Process of synthesizing PEO$_{226}$-*b*-P(FEMA$_{75\%}$-*r*-HEMA$_{25\%}$)$_{100}$

The introduced FEMA units can be crosslinked under the UV irradiation, which can induce structural locking and thus yield a robust polymer matrix. Moreover, the pentafluorobenzene ring of the PFEMA block can participate in π-π interactions with the aromatic ring of phenylalanine anilide. See Figure 1-3. The additional performance of π-π stacking interactions within the interior cavities of imprinted polymer nanospheres can thus greatly increase the selectivity of the imprinted polymer nanospheres for phenylalanine anilide.

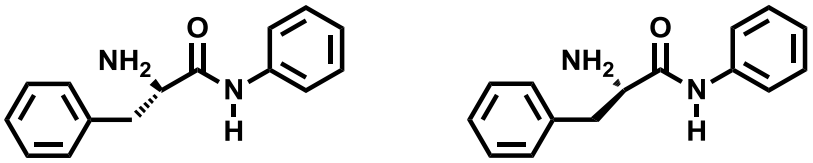

L-phenylalanine anilide D-phenylalanine anilide

Figure 1-2. The chiral template used in this study: 1) D-phenylalanine anilide 2) L-phenylalanine anilide

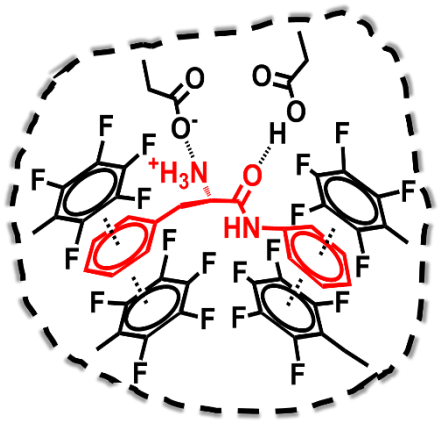

Figure 1-3. The schematic diagram of three types of molecular interactions between the polymer matrix and D-ΦAA molecule.

Chapter 1 will introduce the general background of this subject, including the basic concepts of atom transfer radical polymerization, molecularly imprinted particles, block copolymer self-assembly and the non-covalent interactions that are encountered between the polymer matrix.

Chapter 2 will focus on the synthesis of 2,3,4,5,6-pentafluorocinnamic acid chloride, the step-by-step synthesis of the novel block copolymer, preparation of imprinted polymer nanospheres, and its ability to adsorption of a designed template. ^{1}H-NMR, SEC and UV-vis spectroscopy were employed here to characterize the polymer molecular structure, polymer properties, degree of photocrosslinking of micelles and the sorption amount of imprinted nanospheres. AFM and DLS were employed to analyze the morphology and topology of the micelles prepared.

Chapter 3 will analyze the data collected and summarize the discussion, which includes the characterization of the polymer synthesized, as well as the analysis of the adsorption isotherms and sorption kinetics of template molecules. A comparison was made between two diblock copolymers: PEO_{226}-*b*-$P(FEMA_{75\%}$-*r*-$CA_{25\%})_{100}$ and PEO_{226}-*b*-$P(CEMA_{75\%}$-*r*-$CA_{25\%})_{100}$. The effect of replacing the CEMA units with FEMA units on selectivity and kinetics of MIPs were investigated.

Chapter 4 will provide a general summary of the conclusions reached from this research, highlight the significance of this work, and provide an outline of future work.

1.2 Atom Transfer Radical Polymerization

In recent years there has been significant interest in atom transfer radical polymerization (ATRP), which is newly established controlled radical polymerization method, due to its excellent performance in synthesis of polymers with well-defined composition.[1] Compared to conventional free radical polymerization, polymers synthesized via ATRP usually have a narrower molecular weight distribution.

The basic components of ATRP constitute monomers, initiator with a transferable halogen, catalyst, and ligand. The mechanism of ATRP is shown in Figure 1-4.

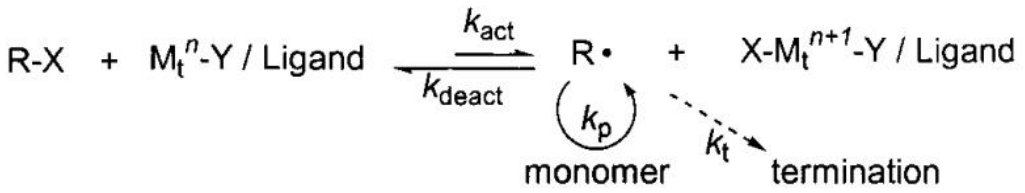

Figure 1-4. Transition-Metal-Catalyzed ATRP [1]

In specifics, a radical generated by transition metal complex will attack the double bond of monomers in the first place, which is the initiation step. Afterwards, the radical can further attract another monomer and lead to chain growth with the constant rate of propagation k_p, this is similar to regular free radical polymerization. Meanwhile, some radicals can get the halogen atom, X back from the metal complex to form the dormant species, with the rate

constant of activation, k_{act} and deactivation k_{deact}. Because of the presence of oxidized metal complex and rapid reversible deactivation, chain termination has been largely controlled and polymer chains can have uniform length. [1,2]

One of the main applications of ATRP is to prepare diblock copolymers with designed architecture and functionalities. Monomers including styrene, methacrylate, methacrylamide and acrylonitrile can be successfully initiated by ATRP initiators and form macroinitiators. The active initiating species formed thus can be used to grow a second block. Block copolymers, such as poly(ethylene oxide)-*block*-poly(2-hydroxyethyl acrylate) can be obtained by this way.

1.3 Molecularly Imprinted Polymer Particles and Their Applications

Molecular imprinting is a multidisciplinary technology that involves the fields of Polymer science, Biochemistry and Chemical Engineering.[5-9] The main objective of molecular imprinting is to prepare a robust polymer matrix possessing numerous internal cavities with specific stereostructure and binding sites by the use of template molecules, so that the imprinted polymer can selectively absorb molecules.[3,10] Molecular imprinting technology (MIT) was first developed in 1972 by Wulff et al.[3,4] and is now widely used for various applications, such as organic separation, chromatography, drug delivery, and various other areas.[5-9]

The basic procedure for producing molecularly imprinted polymer (MIP) nanospheres can be briefly described in three steps, as shown in Figure 1-5. The first step involves the complexing of a functional monomer and a template. Secondly, a robust polymer matrix is prepared using a crosslinker. Functional groups can be arranged and oriented in an orderly pattern during this process. The third step involves the removal of the small template molecules. After template extraction, many internal cavities will remain within polymer matrix with a specific structure and functional group arrangement that can allow selective binding with the template molecules.

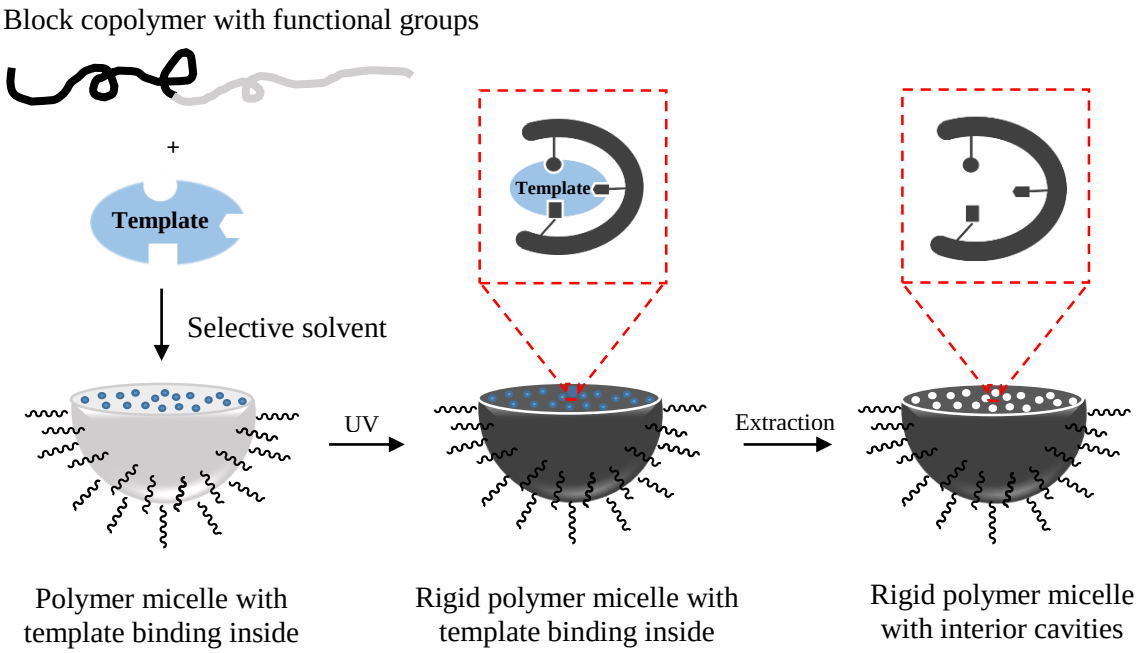

Figure 1-5. Schematic diagram of preparing imprinted polymer nanospheres.

Many researchers have presented qualitative reports describing the theoretical mechanism of molecular imprinting. Nicholls and coworkers reported that the recognition exhibited between MIP particles and template molecules was determined by thermodynamics.[11]

Sellergren analyzed the thermodynamics of the mass transfer of antimers to MIPs.[12] Meanwhile, Chen et al. reported the effect of heat treatment on the mass transfer kinetics.[13]

The change of the Gibbs free energy observed during the formation of a complex between MIPs (ligands) and templates (receptors) can be expressed using the Equation [1-1][9]:

$$\Delta G_{bind} = \Delta G_{t+r} + \Delta G_r + \Delta G_h + \Delta G_{vib} + \Delta G_p + \Delta G_{conf} + \Delta G_{vdw} \quad [1\text{-}1]$$

Where ΔG_{bind} denotes the total Gibbs free energy corresponding to the complex formation, ΔG_{t+r} refers to the translational and rotational energy, and ΔG_r denotes the energy corresponding to the restricted rotation encountered upon complexation. Meanwhile, ΔG_h corresponds to the hydrophobic effect, ΔG_{vib} refers to residual soft vibrational modes, ΔG_p corresponds to the sum of the interacting polar group contributions, ΔG_{conf} denotes adverse conformational changes, and ΔG_{vdw} refers to unfavourable van der Waals interactions.

1.4 Self-Assembly of Amphiphilic Block Copolymer

Self-assembly is a spontaneous process during which molecules can associate together to form elaborate and well-ordered structures due to non-covalent interactions such as hydrogen bonding, electrostatic and van der Waals interactions, as well as various other non-covalent binding modes.[14] As a result of these non-covalent interactions, relatively

simple small molecule or polymeric building blocks can undergo self-assembly to yield highly intricate nanostructures.

Amphiphilic block copolymers often contain two or more distinct blocks with different chemical and physical properties. In the case of a diblock copolymer possessing two blocks, these two blocks are usually thermodynamically incompatible with one another, which can result in phase separation. The phase separation of diblock copolymer can be achieved either in solid state or in solution. When an amphiphilic diblock copolymer is dispersed into a selective solvent at a concentration that exceeds the critical micelle concentration (CMC), the copolymer may self-assemble to form micelles due to differences in the solubility of the constituent blocks. In situations where water is the selective solvent, the poorly soluble hydrophobic block will form the micellar core and the relatively soluble hydrophilic block will stretch into the solvent to form the micellar corona.

Block copolymer micelles can exhibit various morphologies. See Figure 1-6, 1-7. The most commonly encountered morphologies include spherical, cylindrical, and vesicular micelles, but a diverse range of exotic micellar morphologies are also observed, especially in cases involving triblock and multiblock copolymers. Micellar morphologies can be influenced by various factors, such as the solvent composition, the composition of the individual copolymer blocks, the rigidity of the constituent blocks, and the lengths of the copolymer blocks.

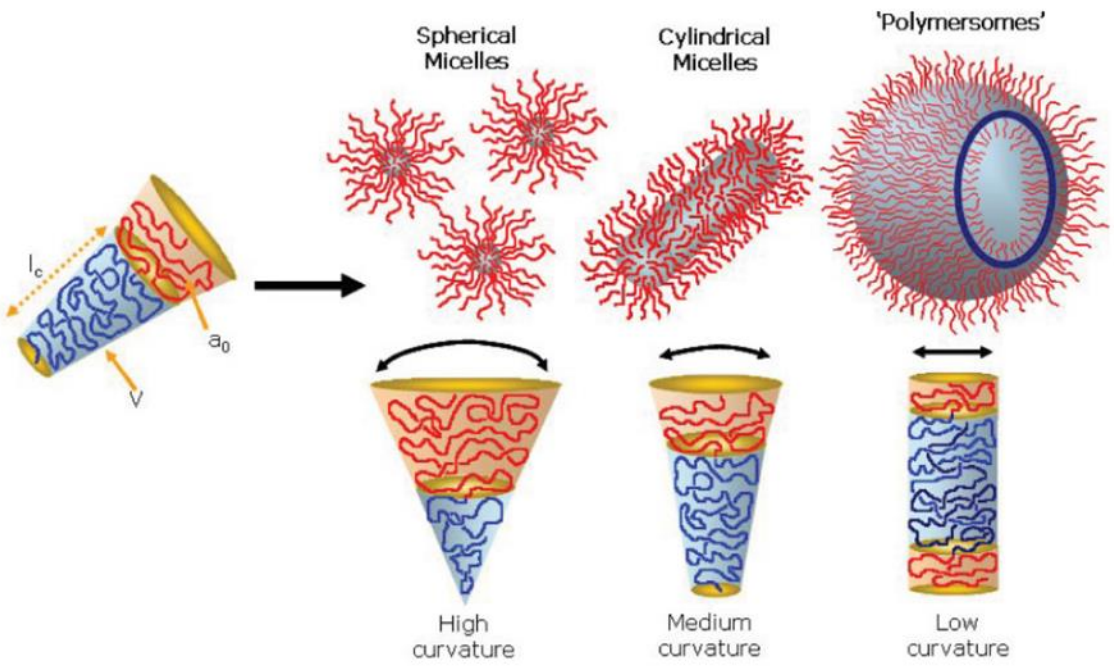

Figure 1-6. Various self-assembled structures formed by amphiphilic block copolymer in a block-selective solvent.[16]

Amphiphilic block copolymer micelles have drawn significant interest from researchers over the years due to their potential applications in microelectronics, drug delivery and surface engineering, and also on account of their high thermodynamic stability.[17-19]

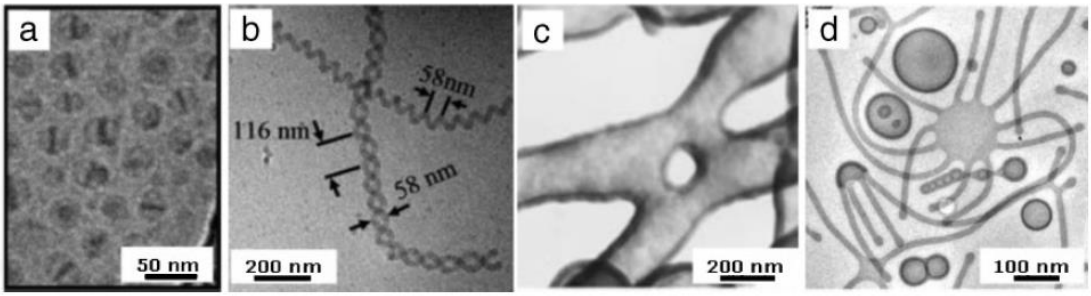

Figure 1-7. Transmission electron micrographs of: a) "hamburger" micelles, b) helical micelles, c) bilayer tubules, and d) mixtures of polymer vesicles and "octopi" structures. [16]

1.5 Non-covalent Interactions: π-π Stacking Interactions

A wide variety of non-covalent molecular interactions are commonly encountered. One commonly observed example is van der Waals interactions, which consist of dispersive and repulsive forces. Another example includes electrostatic interactions, which involve the attraction or repulsion between ions or molecules with permanent charges. Meanwhile, hydrogen bonding is also one type of non-covalent interactions that involves the electronegative atom such as partially negative oxygen, nitrogen and fluorine atom with partially positive hydrogen atom.[20] Other examples include halogen bonding and the solvophobic effect, etc.

π-π stacking interactions were initially discovered in the 1960s and it was demonstrated that they were a new type of non-covalent interaction that are widespread among aromatic compounds. See Figure 1-8. These interactions will occur between the electron clouds of

an aromatic ring bearing an electron acceptor and an aromatic ring with an electron donor.[21-23] This type of non-covalent interaction was demonstrated to be important in crystal engineering.[24]

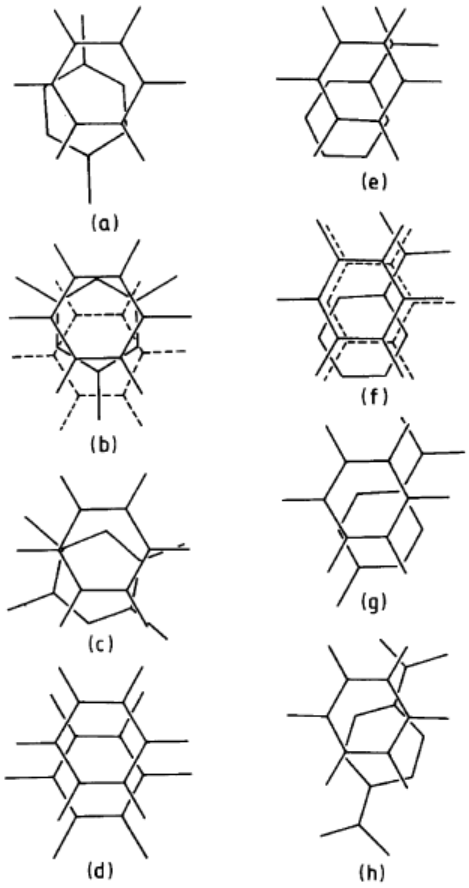

Figure 1-8. Overlap diagram of the hexafluorobenzene complexes of (a) p-xylene, (b) mesitylene, (c) durene, (d) hexamethylbenzene (triclinic form), (e) N,N-dimethylaniline (monoclinic form), (f) N,N-dimethylaniline (triclinic form), (g) N,N-dimethyl-p-toluidine and (h) N,N,N',N'-tetramethylphenylenediamine.[25]

The mechanism of π-π stacking interactions has been a controversial topic. Hamilton reported that the stacking behavior was caused by electrostatic interactions[26]. In contrast, Schneider proposed that the π-π stacking interactions were due to the solvent[27]. Meanwhile, Hunter further revealed an electrostatic model of π-π stacking interactions[28]. In his paper, he reported that electrostatic interactions and van der Waals forces were the two main contributions to the binding model. He also indicated that there were two types of π-π stacking interactions including parallel stacking and perpendicular stacking. The parallel stacking includes face-to-face stacking and offset stacking[28]. See Figure 1-9.

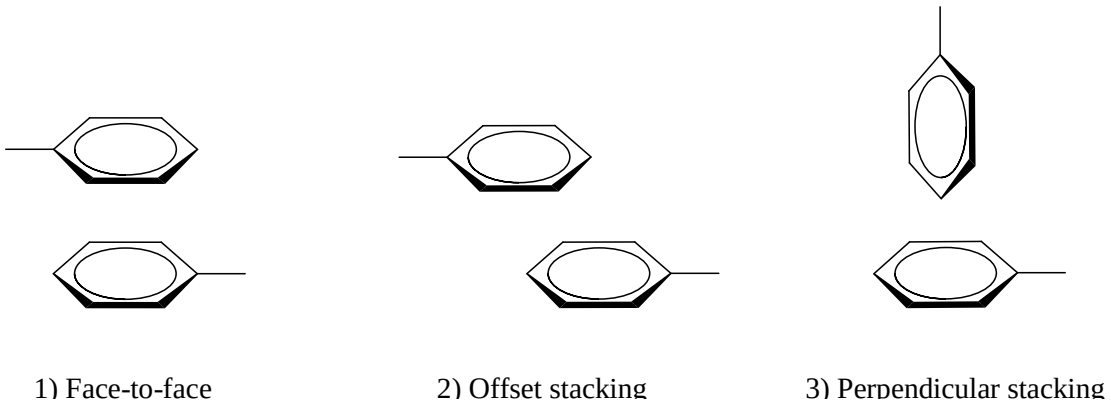

Figure 1-9. Three types of π-π stacking interaction orientation

1.6 Chapter Summary

This chapter has briefly introduce the background concept of atom transfer radical polymerization, diblock copolymer self-assembly in liquids, the process used to prepare molecularly imprinted polymer nanospheres, and the mechanism of π-π stacking interactions.

Chapter 2 will describe the experimental methods to synthesize our target polymer and prepare MIPs. Also the sorption isotherm and sorption kinetics of MIPs prepared will be analyzed and discussed as well.

Reference

1. Matyjaszewski, K.; Xia, *J. Chem. Rev.* **2001**, *101*, 2921-2990.
2. Matyjaszewski, K.; Tsarevsky, N. *Chem. Rev*. **2007**, *107*, 2270-2299.
3. G. Wulff, A. Sarhan, K. Zabrocki, *Tetrahedron Lett.* **1973**, 4329–4332.
4. G. Wulff, A. Sarhan, *Angew. Chem.* **1972**, *84*, 364.
5. G. Wulff, M. Minarik, *HRC & CC, J. High Resolut. Chromatogr. Chromatogr. Commun.* **1986**, *9*, 607–608.
6. B. Sellergren, M. Lepist ö, K. Mosbach, *J. Am. Chem. Soc.* **1988**, *110*, 5853–5860.
7. I. Rubinstein, S. Steinberg, Y. Tor, A. Shanzer, J. Sagiv, *Nature (London)* **1988**, *332*, 426–429.
8. J. Sagiv, *Isr. J. Chem.* **1979**, *18*, 346–353.
9. Ge, Y.; Turner, A. P. F. *Chem.-Eur. J.* **2009**, *15*, 8100–8107
10. Wulff, G. *Chem. Rev.* **2002**, *102*, 1–27.
11. Nicholls IA. *Chem.Lett*., **1995**, *11*, 1035–1036.
12. B. Sellergren, KJ, Shea. *J.Chromatogr*., **1995**, *690*, 29–39.
13. Y. Chen, M. Kele, P. Sajonz, B. Sellergren, *Anal.Chem*., **1999**, *71*, 928–938.
14. S. Zhang, *Biotechnology Advances*, **2002**, *20*, 321.
15. L. Corinne., *Journal of Supramolecular Chemistry*, **2001**, *1*, 39–52.
16. A. Blanazs, S. P. Armes, A. J. Ryan, *Macromol. Rapid Commun.* **2009**, *30*, 267–277.
17. Park, M.; Harrison, C. *Science*, **1997**, *276*, 1401–1404.
18. Yan, X; Liu, G,; Li, Z. *J. Am. Chem. Soc.* **2004**, *12*, 10059–10066.
19. Kataoka, K.; Harada, A. *Adv. Drug Deliv. Rev*. **2001**, *47*, 113–131.
20. E. Arunan, G. R. Desiraju, R. A Klein, J. Sadlej, S. Scheiner, I. Alkorta, D. C. Clary, R. H. Crabtree, J. J. Dannenberg, P. Hobza, H. G. Kjaergaard, A. C. Legon, B. Mennucci, and D. J. Nesbitt. *Pure Appl. Chem*. **2011**, *83*, 1619–1636.
21. Hunter, C. A.; Lawson, K. R.; Perkins, J.; Urch, C. J. *J. Chem. Soc*., Perkin Trans. 2 **2001**, *5*, 651-669.
22. Meyer, E. A.; Castellano, R. K.; Diederich, F. *Angew. Chem., Int. Ed*. **2003**, *42*, 1210-1250.
23. Sinnokrot, M. O.; Sherrill, C. D. *J. Am. Chem. Soc*. **2004**, *126*, 7690-7697.
24. Kool, E. T.; Morales, J. C.; Guckian, K. M. *Angew. Chem., Int. Ed*. **2000**, *39*, 990-1009.
25. Dahl, T. *ACTA Chemica Scandinavica Series A-Physical and Inorganic Chemistry*. **1988**, *42*, 1–7.
26. Zimmerman, S. C.; VanZyl, C. M.; Hamilton, G. S. *J. Am. Chem. Soc*. **1989**, *Ill*, 1373-1381.
27. Schneider, H.-J.; Philippi, K.; PBhlmann, J. *Angew. Chem., Inr. Ed. Engl*. **1984**, *23*, 908-910.
28. Christopher A. Hunter, Jeremy K. M. Sanders *J. Am. Chem. Soc*. **1990**, *112*, 5525-5534

Chapter 2

Experimental Section

2.1 Introduction

This section firstly describes the procedures of synthesis of the target polymer in the following order: 1) synthesis of PEO-Br as the macroinitiator, 2) synthesis of 2-[(trimethylsilyl)oxy]ethyl methacrylate (HEMA-TMS) as the monomer, 3) synthesis of poly(ethylene oxide)-block-poly(hydroxyethylmethacrylate) (PEO-*b*-PHEMA) via atom transfer radical polymerization, 4) synthesis of 2,3,4,5,6-pentafluorocinnamic acid chloride, 5) synthesis of PEO-*b*-P(FEMA-*r*-HEMA), 6) synthesis of PEO-*b*-P(FEMA-*r*-CA). The products synthesized were characterized properly with nuclear magnetic resonance (^{1}H-NMR) and size exclusion chromatography (SEC). The target polymer PEO-*b*-P(FEMA-*r*-CA) was further used to make polymer nanospheres imprinted by D-phenylalanine anilide ($_D$-ΦAA). An experiment was performed to check the selectivity of the prepared polymer nanospheres for D-phenylalanine anilide and L-phenylalanine anilide ($_L$-ΦAA). During the preparation of the polymer nanospheres, atomic force microscopy (AFM) and dynamic light scattering (DLS) were applied in characterizing the morphology and topology of polymer nanospheres prepared. UV-vis spectroscopy was applied to analyze the degree of crosslinking of FEMA and CEMA units and the sorption amount of template.

2.2 Materials

Poly(ethylene oxide) (PEO, M_n = 10,000 g/mol), 2-bromoisobutyryl bromide (98%), triethylamine (99%), hexamethyldisilazane (98%), trimethylsilyl chloride (99%), 2,3,4,5,6-pentafluorocinnamic acid (98%), oxalyl chloride, 1,1,4,7,7-pentamethyldiethylenetriamine (99%), phthalic anhydride (99%), cinnamoyl chloride (98%), dimethylformamide (anhydrous, DMF) and dichloromethane (DCM, Fisher Scientific) were purchased from Aldrich and used as received. 2-Hydroxyethyl methacrylate (97%) was purchased from Aldrich and was distilled in order to remove the inhibitor before use. Copper (I) Bromide (CuBr, 98%) was purchased from Aldrich and washed successively with acetic acid and ethanol prior to use. Pyridine (Fisher Scientific) was refluxed and distilled over CaH_2 under argon. The monomer 2-(trimethylsiloxyl)ethyl methacrylate (HEMA-TMS) was prepared and purified according to a procedure described in the literature. Phenylalanine anilide was synthesized according to previously reported methods. Alanine methyl ester was synthesized and purified from alanine methyl ester hydrochloride (98%), which was purchased from Aldrich.

2.3 Synthesis of PEO_{226}-Br

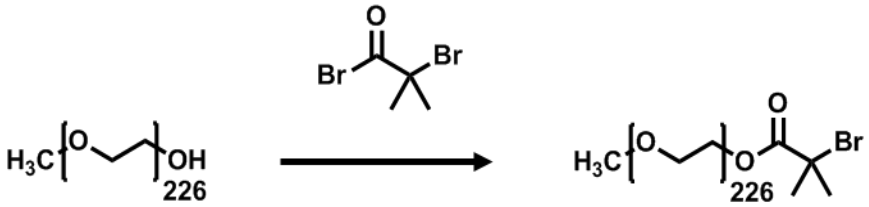

Figure 2-1. Synthesis of PEO_{226}-Br

PEO-OH denotes poly(ethylene glycol) methyl ether. PEO-OH (1.0 g, 0.10 mmol, M_n = 10,000 g/mol) was dried overnight under vacuum at room temperature before it was dissolved in 10 mL of anhydrous toluene in a 50 mL round bottom flask. Triethylamine (5.0×10^{-2} g, 0.50 mmol) was subsequently added into the flask. At room temperature, 0.11 g (0.50 mmol) of 2-bromoisobutyryl bromide was slowly added dropwise into the mixture over 10 min. The flask was sealed and the reaction mixture was stirred at 40 °C for 24 h. The mixture was then filtered to remove the undissolved salt and concentrated by rotary evaporation before it was precipitated from cold diethyl ether. The precipitate was dried under vacuum and redissolved in dichloromethane (DCM). The DCM solution was washed successively with excess amounts of HCl (0.10 M), NaOH (0.10 M) and saturated NaCl solution. The DCM layer was subsequently dried over magnesium sulfate before it was subjected to gravity filtration. This solution was subsequently concentrated via rotary evaporation before it was precipitated from cold diethyl ether. The product was collected by vacuum filtration and was dried overnight under vacuum to yield 0.85 g (83%) of the polymer as a white powder. See Figure 2-1.

2.4 Synthesis of HEMA-TMS

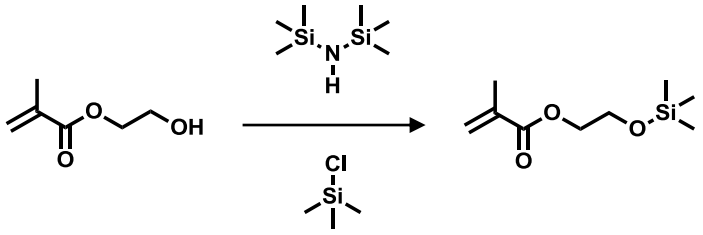

Figure 2-2. Synthesis of HEMA-TMS

The method used to synthesize 2-[(trimethylsilyl)oxy]ethyl methacrylate (denoted as HEMA-TMS) mainly follows the procedures described by Nakahama.[1] Under the protection of nitrogen, 25 g (0.15 mol) of hexamethyldisilazane was added dropwise into 20 g (0.15 mol) of 2-hydroxyethyl methacrylate in a 100 mL round bottom flask, which was immersed in an ice-cold water bath. Trimethylsilyl chloride (0.10 mL) was then added into this flask. The flask was sealed and the reaction mixture was stirred overnight at room temperature. The reaction mixture was then purified via fractional distillation. The distillate was collected at 61 ℃ to yield 22 g (0.13 mol) of the targeted HEMA-TMS as a colorless liquid. See Figure 2-2.

2.5 Synthesis of 2,3,4,5,6-Pentafluorocinnamic Acid Chloride

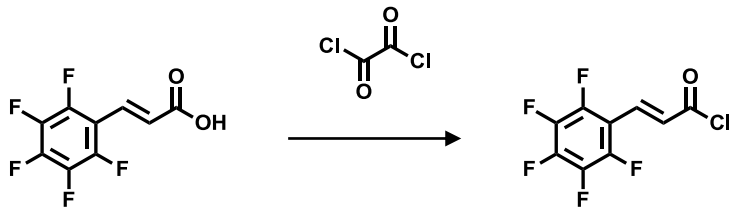

Figure 2-3. Synthesis of 2,3,4,5,6-pentafluorocinnamic acid chloride

2,3,4,5,6-Pentafluorocinnamic acid was dried overnight under vacuum before use. Dried 2,3,4,5,6-pentafluorocinnamic acid (1.0 g, 4.2×10^{-3} mol) was placed into a 50 mL round bottom flask. Oxalyl chloride (3.6 mL, 4.2×10^{-2} mol, in excess amount) was subsequently added dropwise into the flask. The reaction mixture was refluxed overnight at 65 °C under the protection of nitrogen. The reaction solution then underwent rotary evaporation at 45 ℃ for at least 4 h to remove the excess oxalyl chloride and thus yield 0.80 g (73.6%) of 2,3,4,5,6-pentafluorocinnamic acid chloride as a viscous yellow liquid. See Figure 2-3.

2.6 Synthesis of PEO_{226}-*b*-$PHEMA_{100}$

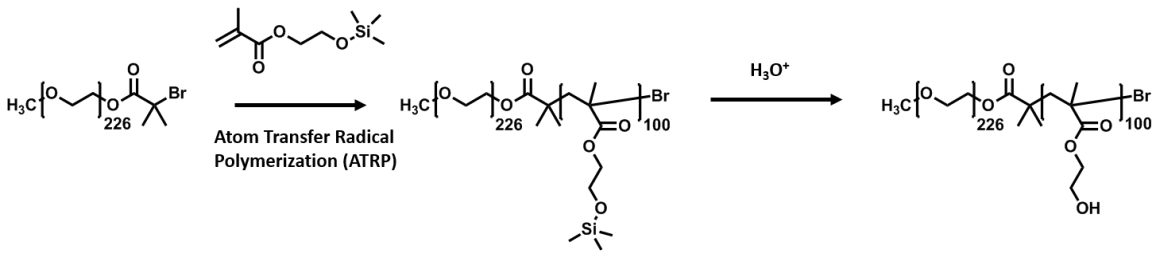

Figure 2-4. Synthesis of PEO_{226}-*b*-$PHEMA_{100}$

In order to synthesize poly(ethylene oxide)-*block*-poly(2-hydroxyethyl methacrylate) (denoted as PEO-*b*-PHEMA), 0.50 g (5.0×10^{-2} mmol) of the macroinitiator PEO-Br and 20.8 μL (0.10 mmol) PMDETA were mixed in 5.0 mL of anhydrous DMF in a dry Schlenk flask. The solution was bubbled for 20 min before 1.41 g (7.0 mmol) of HEMA-TMS and 7.2 mg (5.0×10^{-2} mmol) of CuBr were added into the Schlenk flask. The entire mixture was degassed with three freeze-pump-thaw cycles before the Schlenk flask was immersed into an oil bath at 75 ℃. The reaction solution was stirred for 12 h. In addition, the monomer conversion was monitored via ^{1}H-NMR spectroscopy. The reaction was terminated by the introduction of air and immersing the flask into liquid nitrogen. The reaction solution was subsequently dissolved in THF and passed through a neutral alumina column to remove the copper salt. A 1.0 M HCl solution (1.0 mL) was added into the collected THF elution after it had been concentrated by rotary evaporation. The solution was stirred for 24 h before it was precipitated via addition into an excess of cold diethyl ether. The whitish powder was collected by vacuum filtration and dried under vacuum, thus yielding 1.02 g of PEO_{226}-*b*-$PHEMA_{100}$ as a white powder in an 89% yield. See Figure 2-4.

2.7 Synthesis of PEO_{226}-*b*-P($FEMA_{75\%}$-*r*-$HEMA_{25\%}$)$_{100}$

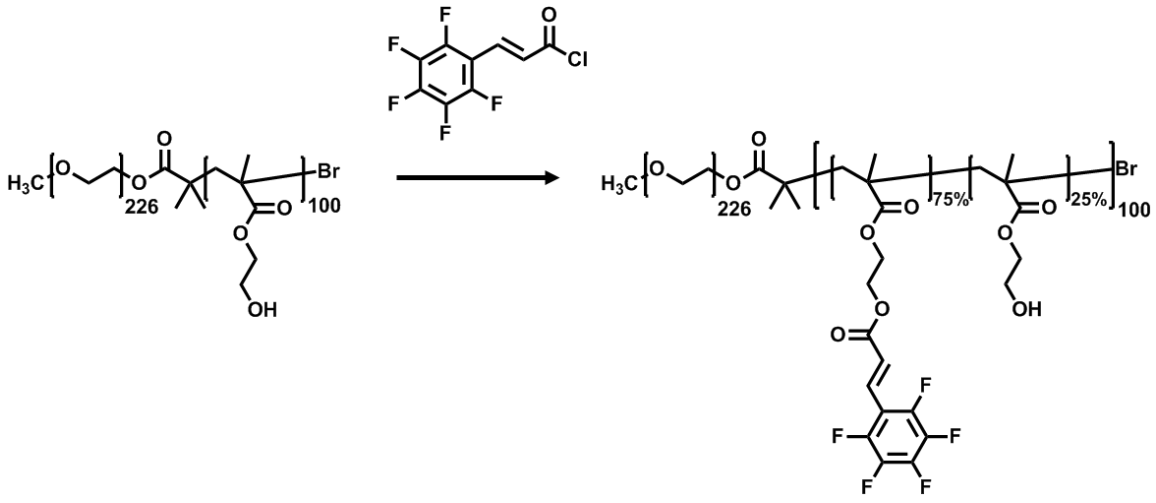

Figure 2-5 Synthesis of PEO_{226}-*b*-P($FEMA_{75\%}$-*r*-$HEMA_{25\%}$)$_{100}$

In order to prepare PEO_{226}-*b*-P($FEMA_{75\%}$-*r*-$HEMA_{25\%}$)$_{100}$, its precursor PEO_{226}-*b*-$PHEMA_{100}$ was initially dried overnight under vacuum prior to use. The dried PEO_{226}-*b*-$PHEMA_{100}$ (1.0 g, 4.0×10^{-2} mmol) was dissolved in 5.0 mL of anhydrous pyridine in a 20 mL scintillation vial. 2,3,4,5,6-Pentafluorocinnamic acid chloride (0.90 g, 3.54 mmol) was added dropwise into the pyridine solution under vigorous stirring. The vial was sealed and the reaction mixture was stirred in the dark overnight at room temperature. The reaction process was monitored via ^{1}H-NMR spectroscopy. The final amount of 2,3,4,5,6-pentafluorocinnamic acid chloride added was determined by the target degree of acylation. After the degree of acylation achieved 75%, the reaction solution was subsequently dialyzed against 50 mL of methanol to remove the pyridine hydrochloride. The external methanol solution was changed four times over three days. The internal suspension was further concentrated by rotary evaporation and precipitated from an excess of cold diethyl ether. The yellowish product was collected by vacuum filtration and dried under vacuum,

thus providing 1.53 g of PEO_{226}-*b*-$P(FEMA_{75\%}$-*r*-$HEMA_{25\%})_{100}$ in an 89% yield. See Figure 2-5.

2.8 Synthesis of PEO_{226}-*b*-$P(CEMA_{75\%}$-*r*-$HEMA_{25\%})_{100}$

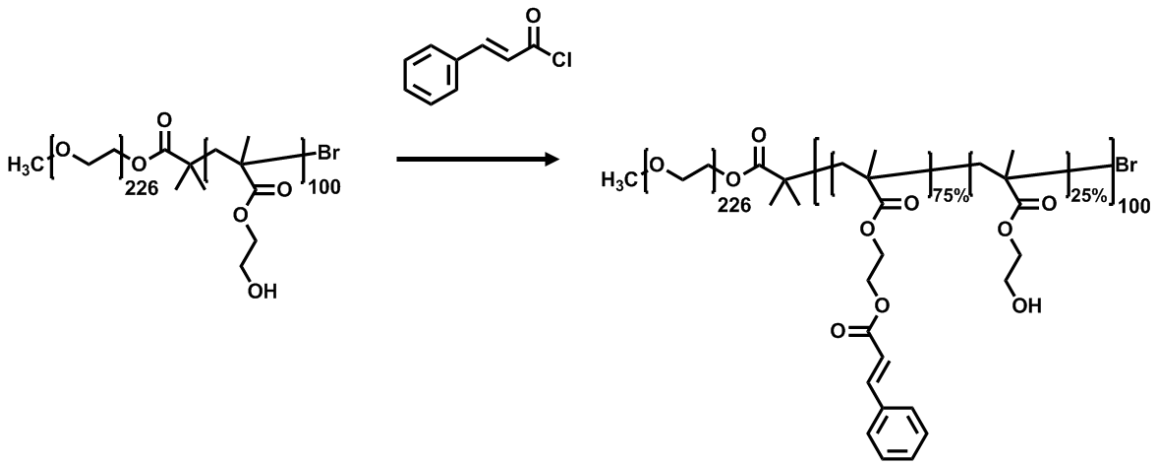

Figure 2-6. Synthesis of PEO_{226}-*b*-$P(CEMA_{75\%}$-*r*-$HEMA_{25\%})_{100}$

In order to prepare PEO_{226}-*b*-$P(CEMA_{75\%}$-*r*-$HEMA_{25\%})_{100}$, its precursor PEO_{226}-*b*-$PHEMA_{100}$ was initially dried overnight under vacuum prior to use. The dried PEO_{226}-*b*-$PHEMA_{100}$ (1.0 g, 4.0×10^{-2} mmol) was dissolved in 5.0 mL of anhydrous pyridine in a 20 mL scintillation vial. Cinnamoyl chloride (0.50 g, 3.0 mmol) was added into another 5.0 mL pyridine solution. The 5.0 mL pyridine suspension with cinnamoyl chloride was then added dropwise into the 5.0 mL pyridine solution with polymer under vigorously stirring. The vial was sealed and the reaction mixture was stirred in the dark overnight at room temperature. The reaction process was monitored via ^{1}H-NMR spectroscopy. The final amount of cinnamoyl chloride added was determined by the target degree of acylation.

After the degree of acylation achieved 75%, the reaction solution was subsequently dialyzed against 50 mL of methanol to remove the pyridine hydrochloride. The external methanol solution was changed four times over three days. The internal suspension was further concentrated by rotary evaporation and precipitated from an excess of cold diethyl ether. The yellowish product was collected by vacuum filtration and dried under vacuum, thus providing 1.24 g of PEO_{226}-*b*-P($CEMA_{75\%}$-*r*-$HEMA_{25\%}$)$_{100}$. See Figure 2-6.

2.9 Synthesis of PEO_{226}-*b*-P($CEMA_{75\%}$-*r*-$CA_{25\%}$)$_{100}$

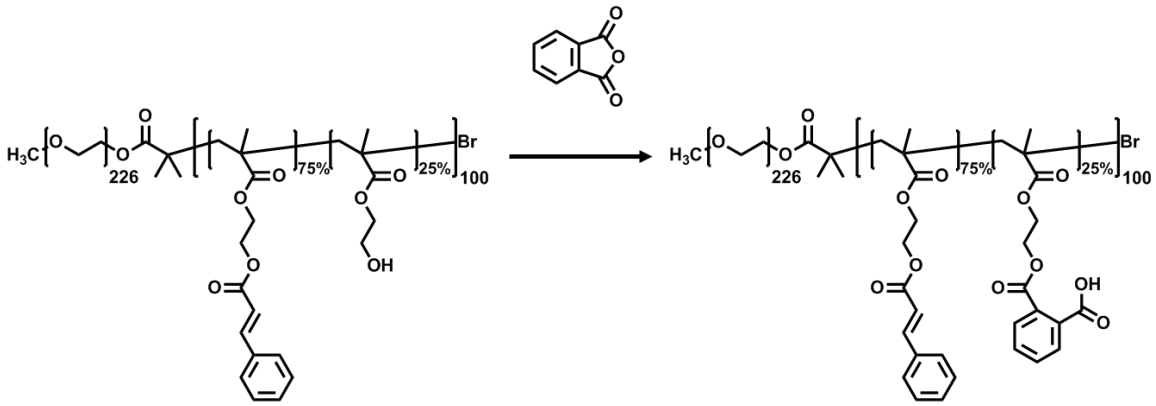

Figure 2-7. Synthesis of PEO_{226}-*b*-P($CEMA_{75\%}$-*r*-$CA_{25\%}$)$_{100}$

In order to prepare PEO_{226}-*b*-P($CEMA_{75\%}$-*r*-$CA_{25\%}$)$_{100}$, PEO_{226}-*b*-P($CEMA_{75\%}$-*r*-$HEMA_{25\%}$)$_{100}$ was dried under vacuum overnight prior to use. The dried PEO_{226}-*b*-P($CEMA_{75\%}$-*r*-$HEMA_{25\%}$)$_{100}$ (1.2 g, 3.7×10^{-2} mmol) was dissolved into 8.0 mL of anhydrous pyridine in a 20 mL scintillation vial. Subsequently 1.36 g (9.16 mmol, an excess amount) of phthalic anhydride was added into the pyridine solution. The vial was sealed and the reaction mixture was stirred in the dark overnight at room temperature. The

progress of reaction was monitored via ^{1}H-NMR spectroscopy. The reaction mixture was subsequently dialyzed against 50 mL of methanol to remove the pyridine hydrochloride and excess phthalic anhydride. The external methanol solution was changed four times over three days. The interior suspension was subsequently concentrated by rotary evaporation and precipitated into excess 0.10 M HCl solution and then washed three times (3×50 mL) with 0.10 M HCl. The yellowish flaky product was collected by vacuum filtration and dried under vacuum, to provide 1.15 g of PEO_{226}-*b*-P($CEMA_{75\%}$-*r*-$CA_{25\%}$)$_{100}$. See Figure 2-7.

2.10 Synthesis of PEO_{226}-*b*-P($FEMA_{75\%}$-*r*-$CA_{25\%}$)$_{100}$

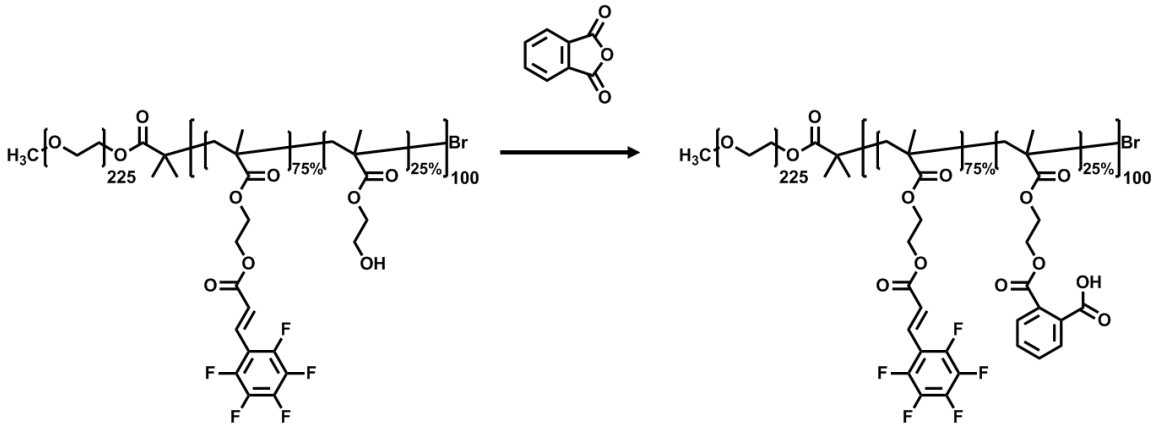

Figure 2-8. Synthesis of PEO_{226}-*b*-P($FEMA_{75\%}$-*r*-$CA_{25\%}$)$_{100}$

In order to prepare PEO_{226}-*b*-P($FEMA_{75\%}$-*r*-$CA_{25\%}$)$_{100}$, PEO_{226}-*b*-P($FEMA_{75\%}$-*r*-$HEMA_{25\%}$)$_{100}$ was dried under vacuum overnight prior to use. The dried PEO_{226}-*b*-P($FEMA_{75\%}$-*r*-$HEMA_{25\%}$)$_{100}$ (1.50 g, 4.0×10^{-2} mmol) was dissolved into 8.0 mL of

anhydrous pyridine in a 20 mL scintillation vial. Subsequently 1.41 g (9.49 mmol, an excess amount) of phthalic anhydride was added into the pyridine solution. The vial was sealed and the reaction mixture was stirred in the dark overnight at room temperature. The progress of reaction was monitored via ^{1}H-NMR spectroscopy. The reaction mixture was subsequently dialyzed against 50 mL of methanol to remove the pyridine hydrochloride and excess phthalic anhydride. The external methanol solution was changed four times over three days. The interior suspension was subsequently concentrated by rotary evaporation and precipitated into excess 0.10 M HCl solution and then washed three times (3×50 mL) with 0.10 M HCl. The yellowish flaky product was collected by vacuum filtration and dried under vacuum, to provide 1.48 g of PEO_{226}-*b*-$P(FEMA_{75\%}$-*r*-$CA_{25\%})_{100}$ in a 90.2% yield. See Figure 2-8.

2.11 Preparation of *D*-ΦAA-Imprinted PEO_{226}-*b*-$P(FEMA_{75\%}$-*r*-$CA_{25\%})_{100}$ Nanospheres.

PEO_{226}-*b*-$P(FEMA_{75\%}$-*r*-$CA_{25\%})_{100}$ (50 mg, bearing 25 μmol of carboxylic groups) and 1.5 mg (6.3 μmol) of *D*-phenylalanine anilide (*D*-ΦAA) were dissolved in 0.50 mL of chloroform. The solution was stirred and equilibrated for 6 h. Methanol (9.5 mL) was then added dropwise with a pump into the chloroform solution over a 1 h period under vigorous stirring. The micellar solution was formed and equilibrated overnight before it was irradiated for 2.5 h to achieve a 70% degree of crosslinking of FEMA units. This micellar solution was then concentrated to 2.0 mL and dialyzed against 50 mL of a methanol/chloroform mixture at v/v = 2:8 in order to remove the *D*-ΦAA template. UV

spectroscopy was used to determine the amount of imprinted molecules in the external solution mixture. When the absorbance reading at 242 nm in methanol become negligible, the interior solution was further concentrated and precipitated into excess cold diethyl ether. The residue in external solution was collected after rotary evaporation and dissolved in methanol. Based on the data collected from control experiment with only 1.5 mg $_D$-ΦAA dissolved in methanol, the amount of template extracted was quantified from the absorbance at 242 nm. The precipitate was dried under vacuum and stored at 4 ℃.

2.12 Analysis of the Sorption Isotherms

In order to analyze the sorption isotherms of $_D$-ΦAA and $_L$-ΦAA, 10 mg of the polymer nanospheres that had been imprinted with $_D$-ΦAA was dissolved in 1.0 mL of chloroform. The suspension was transferred into a dialysis tube with M_w cut-off values of 1,2000-1,4000 g/mol. The dialysis tube was immersed into a 20 mL scintillation vial containing 9.0 mL of chloroform bearing a given amount of dissolved imprinting molecules (0.50 to 6.5 mM). The vial was sealed and the system was equilibrated overnight. The concentration of the $_D$-ΦAA or $_L$-ΦAA imprinting molecules in the external chloroform solution was quantified via UV-vis spectroscopy in chloroform. By comparison with a standard experiment performed in the absence of imprinted polymer nanospheres, the amount of imprinting molecules could be calculated by the decrease in the UV absorbance reading at 240 nm. The experiment was repeated for three times.

2.13 Analysis of the Sorption Kinetics

In order to analyze the sorption kinetics of $_D$-ΦAA, 10 mg of the polymer nanospheres that had been imprinted with $_D$-ΦAA was dissolved in 1.0 mL of chloroform. The suspension was transferred into a dialysis tube with M_w cut-off values of 1,2000-1, 4000 g/mol. The dialysis tube was immersed into a 20 mL scintillation vial containing 9.0 mL of chloroform bearing a given amount of dissolved $_D$-ΦAA (6.5 mM). The vial was sealed and the data acquisition was started after 10 min equilibration. The concentration of the $_D$-ΦAA imprinting molecules in the external chloroform solution was quantified via UV-vis spectroscopy in chloroform. By comparison with a standard experiment performed in the absence of imprinted polymer nanospheres, the amount of imprinting molecules could be calculated by the decrease in the UV absorbance reading at 240 nm. The experiment was repeated for three times.

2.14 Instruments and Techniques

^{1}H-NMR measurements were conducted using Bruker Avance-300. UV-vis spectroscopy was performed with a Varian-300 UV-visible spectrophotometer using 1.00 cm Hellma quartz cells. Molecular weights and polydispersity indices were determined via size exclusion chromatography (SEC) measurements, which were performed using a Wyatt instrument that was equipped with an Optilab rEX refractive index detector. Dimethylformamide was used as the eluent at a flow rate of 0.8 mL/min. Light scattering measurements were performed on a Brookhaven BI-200SM Goniometer with a BI-9000AT digital correlator. Micellar solution was prepared in v/v = 0.5/9.5 methanol/chloroform mixture with a concentration ~0.1 mg/mL. The micellar solution was then used for dynamic light scattering at a scattering angle of 90 °. The sample was clarified by passing through 0.22 μm filter. Atomic Force Microscopy images were recorded using a Veeco quadrexed Multimode III with a J vertical scanner. Samples were aspirated from methanol/chloroform mixture at v/v = 0.5/9.5.

2.15 Chapter Summary

In this chapter, we synthesized PEO_{226}-*b*-$P(FEMA_{75\%}$-*r*-$CA_{25\%})_{100}$ and PEO_{226}-*b*-$P(CEMA_{75\%}$-*r*-$CA_{25\%})_{100}$ step by step. Two of these diblock copolymers mixed with $_{D}$-ΦAA were further made as micellar solutions at the same polymer concentration. The two types of micelles were then irradiated to lock the core of the micelles. The $_{D}$-ΦAA was then

extracted from the crosslinked micelles to yield polymer nanospheres. The prepared polymer nanospheres were used in the nest step to analyze their sorption isotherms of $_D$-ΦAA and $_L$-ΦAA. The sorption kinetics of PEO_{226}-*b*-$P(FEMA_{75\%}$-*r*-$CA_{25\%})_{100}$ and PEO_{226}-*b*-$P(CEMA_{75\%}$-*r*-$CA_{25\%})_{100}$ for $_D$-ΦAA were also investigated.

In the characterization part, H-NMR and SEC were employed to study the structures and properties of the polymers synthesized. After the preparation of micellar solution, AFM and DLS were employed to study the morphology, topology and hydrodynamic diameters of crosslinked micelles. The UV-vis spectroscopy was applied to analyze the degree of crosslinking of FEMA and CEMA units. The sorption amount of template can also be detected by this way.

Reference

1. Akira Hirao; Seiichi Nakahama, *Macromolecules* **1986**, *19*, 1294-1299.

Chapter 3

Results and Discussion

3.1 Introduction

This chapter focuses on the polymer characterization, morphology studies of PEO_{226}-*b*-$P(FEMA_{75\%}$-*r*-$HEMA_{25\%})_{100}$ nanospheres, sorption isotherm of $_D$-ΦAA and $_L$-ΦAA for PEO_{226}-*b*-$P(FEMA_{75\%}$-*r*-$HEMA_{25\%})_{100}$ and PEO_{226}-*b*-$P(CEMA_{75\%}$-*r*-$HEMA_{25\%})_{100}$ nanospheres and the sorption kinetics studies of $_D$-ΦAA for PEO_{226}-*b*-$P(FEMA_{75\%}$-*r*-$HEMA_{25\%})_{100}$ nanospheres. To characterize the polymer synthesized, ^{1}H-NMR and SEC were employed. To visualize the morphology of nanospheres, AFM was employed. To analyze the polydispersity and determine the hydrodynamic diameters of the nanospheres, DLS was employed. To study the sorption isotherm and sorption kinetics, UV-vis spectroscopy was employed.

3.2 Polymer Characterization

PEO-OH was terminated by 2-bromoisobutyryl bromide. Triethylamine was added to react with the HBr produced by the reaction in order to shift the reaction equilibrium to the right and thus ensure the complete consumption of the reagents. Triethylamine hydrobromide is insoluble in toluene so that it could be readily removed by filtration. The

polymer product after purification was characterized by ^{1}H-NMR spectroscopy. In comparison with the ^{1}H-NMR spectrum of PEO-OH, two new peaks were visible in the spectrum of PEO-Br. The new signal at 4.4 ppm corresponded to the two protons adjacent to the oxygen atom connected to the carbonyl group of 2-bromoisobutyryl bromide. Meanwhile, the signal observed around 1.8 - 1.9 ppm corresponded to the six protons of the two methyl groups of 2-bromoisobutyryl bromide. The integration ratio of these two new groups was very close to 1:3 (-CH_2- : 2-CH_3), which confirmed that the 2-bromoisobutyryl bromide was successfully reacted with PEO-OH and all of the PEO-OH has been fully terminated. See Figure 3-1.

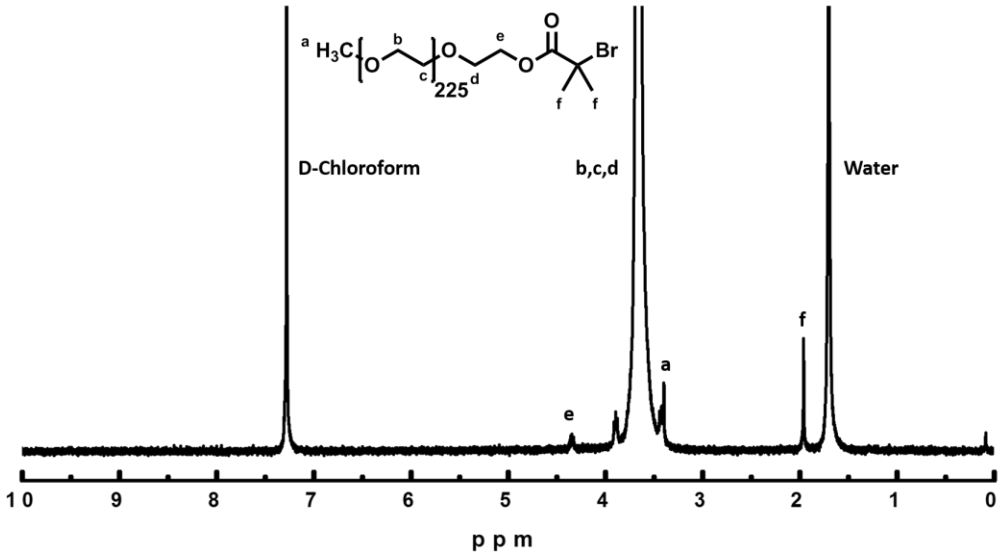

Figure 3-1. ^{1}H-NMR spectrum of macroinitiator PEO-Br in $CDCl_3$

PEO-*b*-PHEMA-TMS was synthesized via atom transfer radical polymerization (ATRP). Here, PEO-Br was used as the macroinitiator, HEMA-TMS as the monomer, CuBr as a catalyst and PMDETA as a ligand. The feed ratio of the four reagents was 1:140:1:2,

respectively. HEMA-TMS readily undergoes hydrolysis, so care was taken to ensure that the flask was sufficiently dry and that the DMF was anhydrous. The reaction mixture of ATRP was frozen and thawed three times to remove the oxygen, thus avoiding the oxidization of copper (I) and the quenching of radicals. During the reaction process, small samples were periodically collected from the flask and characterized by ^{1}H-NMR spectroscopy. The degree of monomer conversion could be calculated by the decrease in the integrations of the two signals at 5.0 and 6.4 ppm observed in *d*-methanol corresponding to the two protons of the HEMA-TMS double bond. According to the ^{1}H-NMR spectrum of the reaction mixture, the monomer conversion was calculated as 71% after 12 h. This indicated that the HEMA-TMS block had approximately 100 repeating units.

The purpose of introducing the –TMS protection group was to prevent the crosslinking of HEMA and to decrease the polydispersity (PDI) of the resultant PEO-*b*-PHEMA copolymer. During the purification process, an HCl solution was added in order to hydrolyze the HEMA-TMS and thus remove the –TMS group. After this purification, the polymer was characterized by SEC and ^{1}H-NMR spectroscopy. The SEC chromatography revealed that the peak corresponding to PEO-Br at 19~20 min had disappeared and was replaced by a new peak at 18~19 min. This indicated that the HEMA-TMS has been successfully initiated and had undergone polymerization. Besides the single peak observed at 18 min, there were no other peaks in the SEC spectrum, which demonstrated that all of the PEO-Br chains had been initiated and the initiation efficiency was near 100%. The PDI of the synthesized block copolymer was 1.18. (Figure 3-2, 3-3).

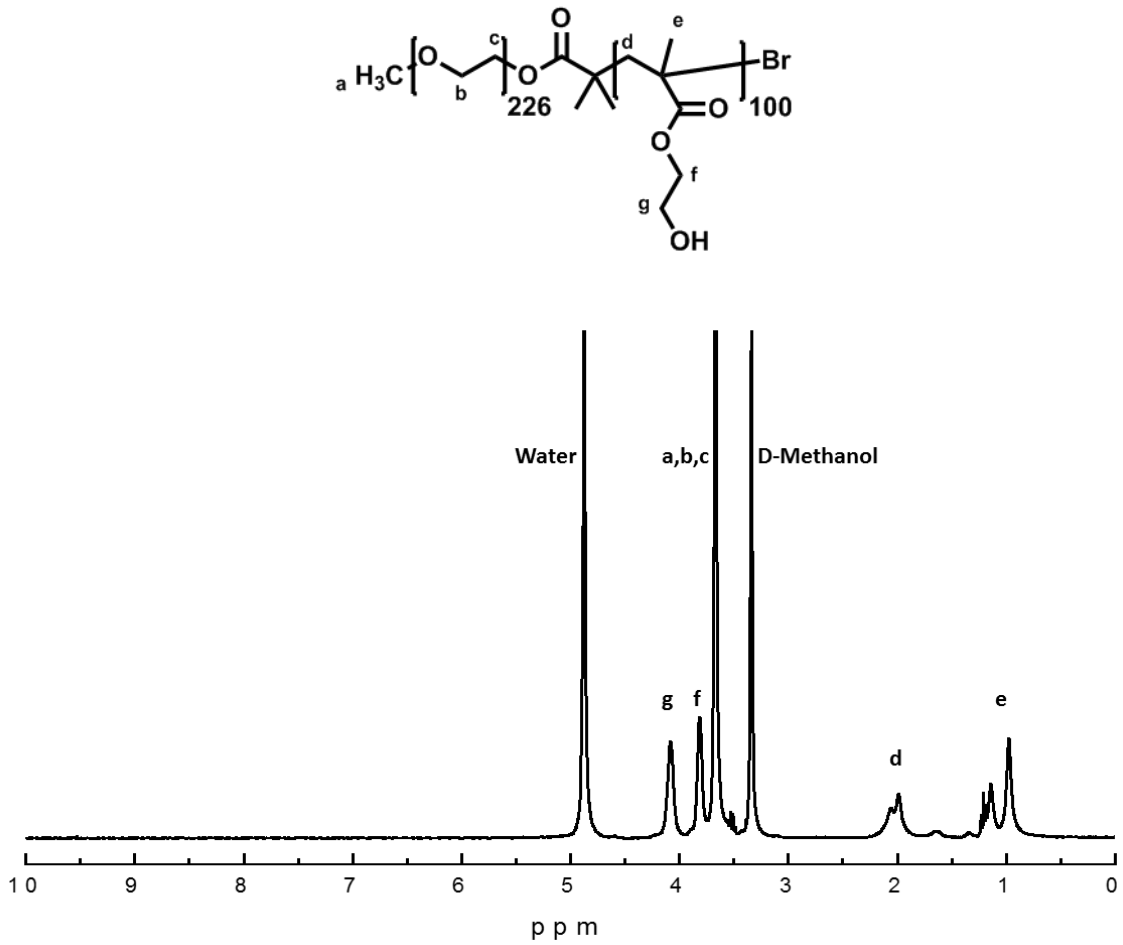

Figure 3-2. ^{1}H-NMR spectrum of block copolymer PEO-*b*-PHEMA in CD_3OD

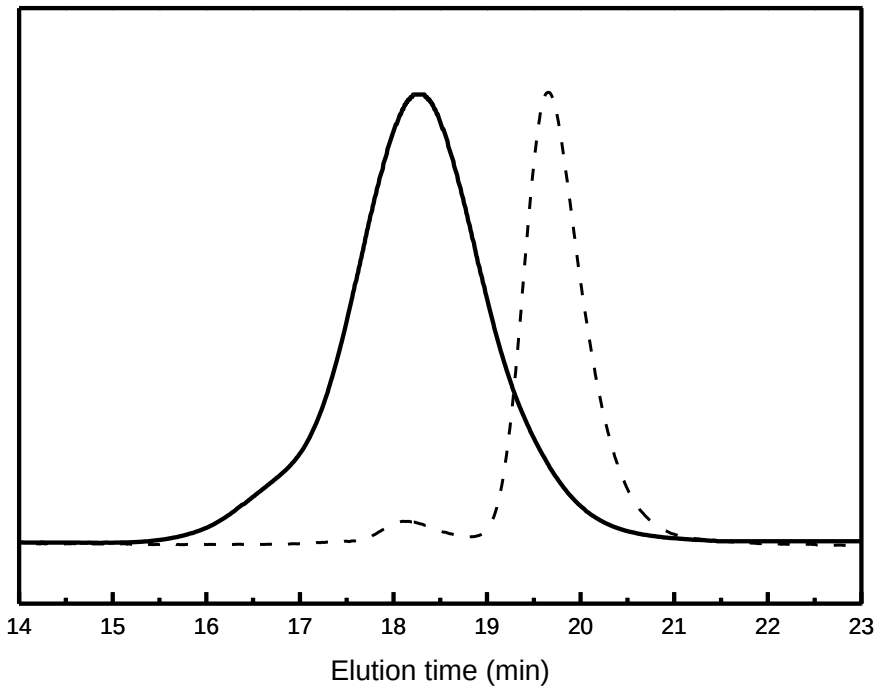

Figure 3-3. SEC traces of macroinitiator PEO-Br (dashed) and block copolymer PEO-*b*-PHEMA (bold)

In order to prepare 2,3,4,5,6-pentafluorocinnamic acid chloride, 2,3,4,5,6-pentafluorocinnamic acid underwent a nucleophilic addition reaction with oxalyl chloride, as shown in Figure 3-4. In addition to 2,3,4,5,6-pentafluorocinnamic acid chloride, the other products produced by this reaction included CO_2, CO and HCl. The boiling point of oxalyl chloride was 62-65 ℃ (lit), and thus it could be readily removed under vacuum. The synthesized 2,3,4,5,6-pentafluorocinnamic acid chloride was used immediately after preparation as a reagent for the next step without further characterization.

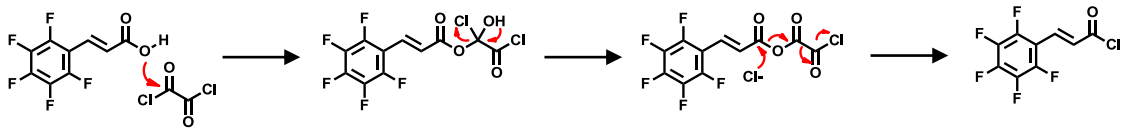

Figure 3-4. Mechanism of nucleophilic addition reaction of pentafluorocinnamic acid

To prepare PEO-*b*-P(FEMA-*r*-PCA), PEO-*b*-PHEMA was reacted with pentafluorocinnamic acid chloride and phthalic anhydride. During the first step of this chemical modification, a given amount of pentafluorocinnamic acid chloride was added into an anhydrous pyridine solution of the polymer under vigorous stirring. The PHEMA block's hydroxyl groups could easily react with the acid chloride. The acid chloride was added dropwise into the polymer solution instead of in the reverse order to ensure that each polymer chain underwent consistent acylation. Performing the addition in this order reduced the possibility that some PHEMA chains underwent complete acylation, while the degree of acylation among the other chains was low. The determination of the amount of pentafluorocinnamic acid chloride added was based on the degree of acylation, which is expected to be approximately 75%.

The reaction mixture was dialyzed against methanol and precipitated in diethyl ether to fully remove the pyridine hydrochloride along with other impurities. The purity of the polymer was characterized via thin-layer chromatography (TLC) and by ^{1}H-NMR spectroscopy. In addition to signals corresponding to PEO-*b*-PHEMA, the ^{1}H-NMR

spectrum of the product obtained after the first modification step also exhibited signals at 6.7 and 7.6 ppm. These two signals corresponded to the two protons of the double bond of FEMA units. In comparison with the sharp and narrow peaks typically observed in the ^{1}H-NMR spectra of small molecules, polymers usually exhibit relatively broad NMR signals. This broadening behaviour was also exhibited by these signals (See Figure 3-6), which suggested that the pentafluorocinnamic acid chloride had been successfully reacted with the hydroxyl groups of the HEMA block. The integration of the two peaks relative to the backbone of PEO revealed that approximately 75% of the hydroxyl groups of the HEMA unit had undergone acylation. The feed ratio of the hydroxyl groups of the PHEMA block to the pentafluorocinnamic acid chloride added was 1:0.885. These results revealed that the reaction efficiency of the pentafluorocinnamic acid chloride synthesized was 84.7% (Figure 3-6).

During the second step of the chemical modification, a given amount of PEO_{226}-*b*-$P(FEMA_{75\%}$-*r*-$HEMA_{25\%})_{100}$ was reacted with an excess amount of phthalic anhydride. The hydroxyl groups could readily react with the phthalic anhydride to undergo a ring-opening reaction. The reaction process was monitored by ^{1}H-NMR spectroscopy. The dialysis procedure helped remove the pyridine salt as well as other impurities. The polymer was further precipitated from a 0.1 M HCl (pH = 1) solution to ensure that all of the carboxyl groups (pK_a = 4.2) had been fully protonated. The ATR-IR spectrum of the product confirmed that all of the $–COO^-$ groups had been converted to –COOH groups (1720.37 cm^{-1}), as shown in Figure 3-5. According to the ^{1}H-NMR spectrum of the polymer product collected, the protons of the remaining $–CH_2$-CH_2- group (Figure 3-5, j

and k) on the PHEMA block had completely shifted to 4-4.5 ppm (Figure 3-7, j and k) and the aromatic protons were observed at approximately 7.5-8.0 ppm, which confirmed that the remaining hydroxyl groups of the PHEMA block, which represented 25% of all of chains, had undergone a quantitative reaction with the phthalic anhydride. See Figure 3-7.

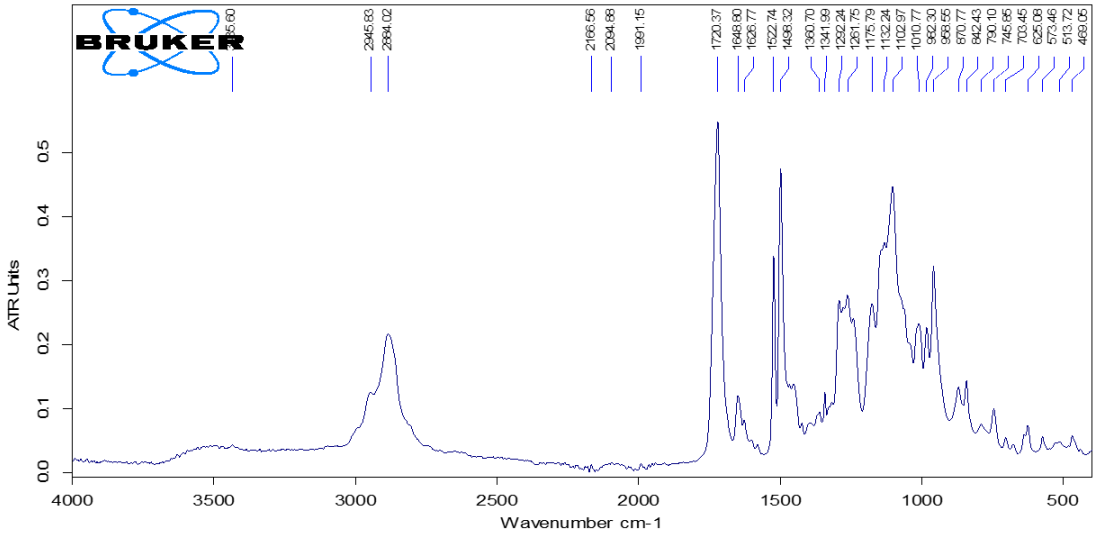

Figure 3-5. ATR-IR spectrum of PEO-*b*-P(FEMA-*r*-CA)

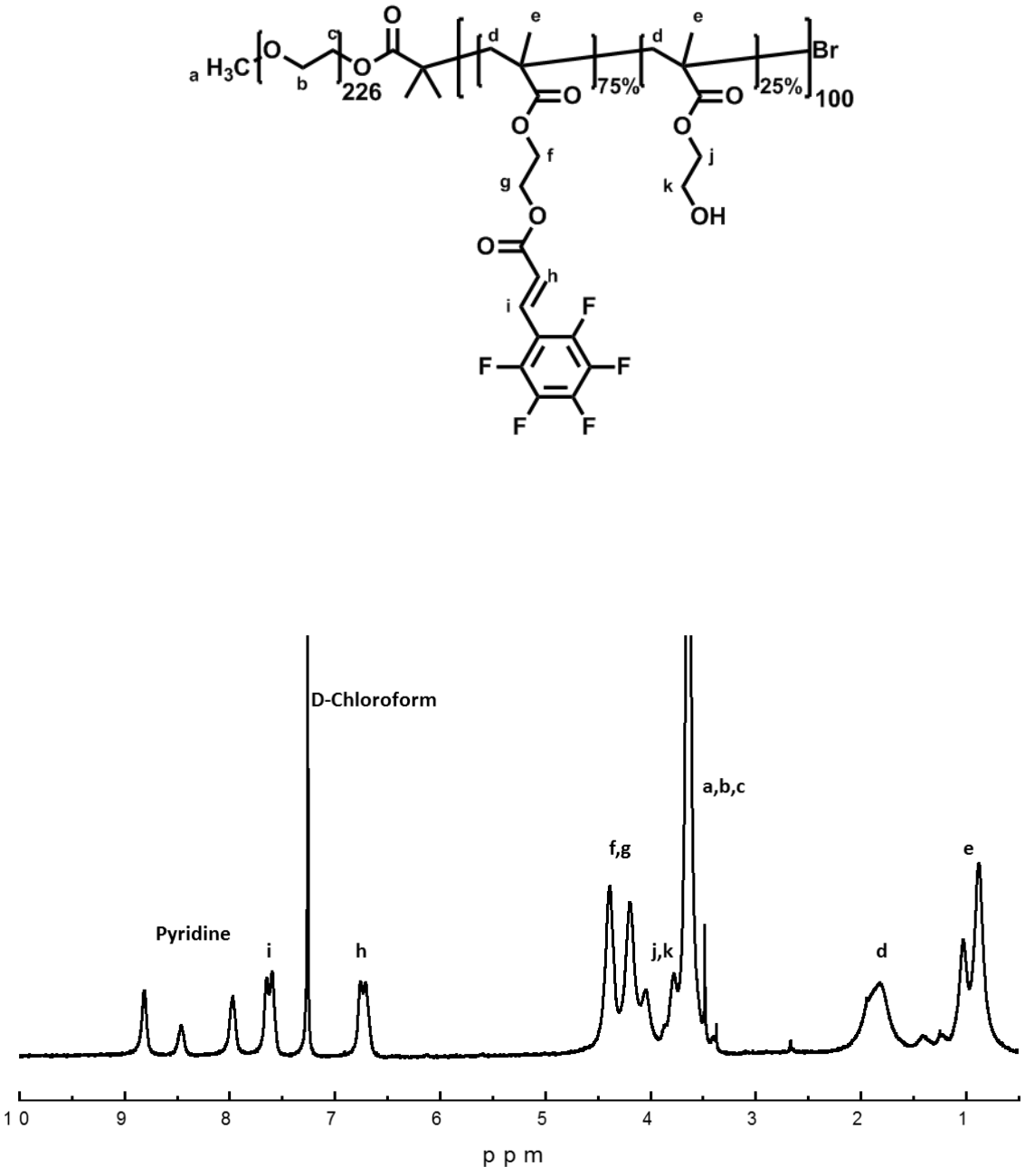

Figure 3-6. ^{1}H-NMR spectrum of block copolymer PEO$_{226}$-*b*-P(FEMA$_{75\%}$-*r*-HEMA$_{25\%}$)$_{100}$ in CDCl$_3$

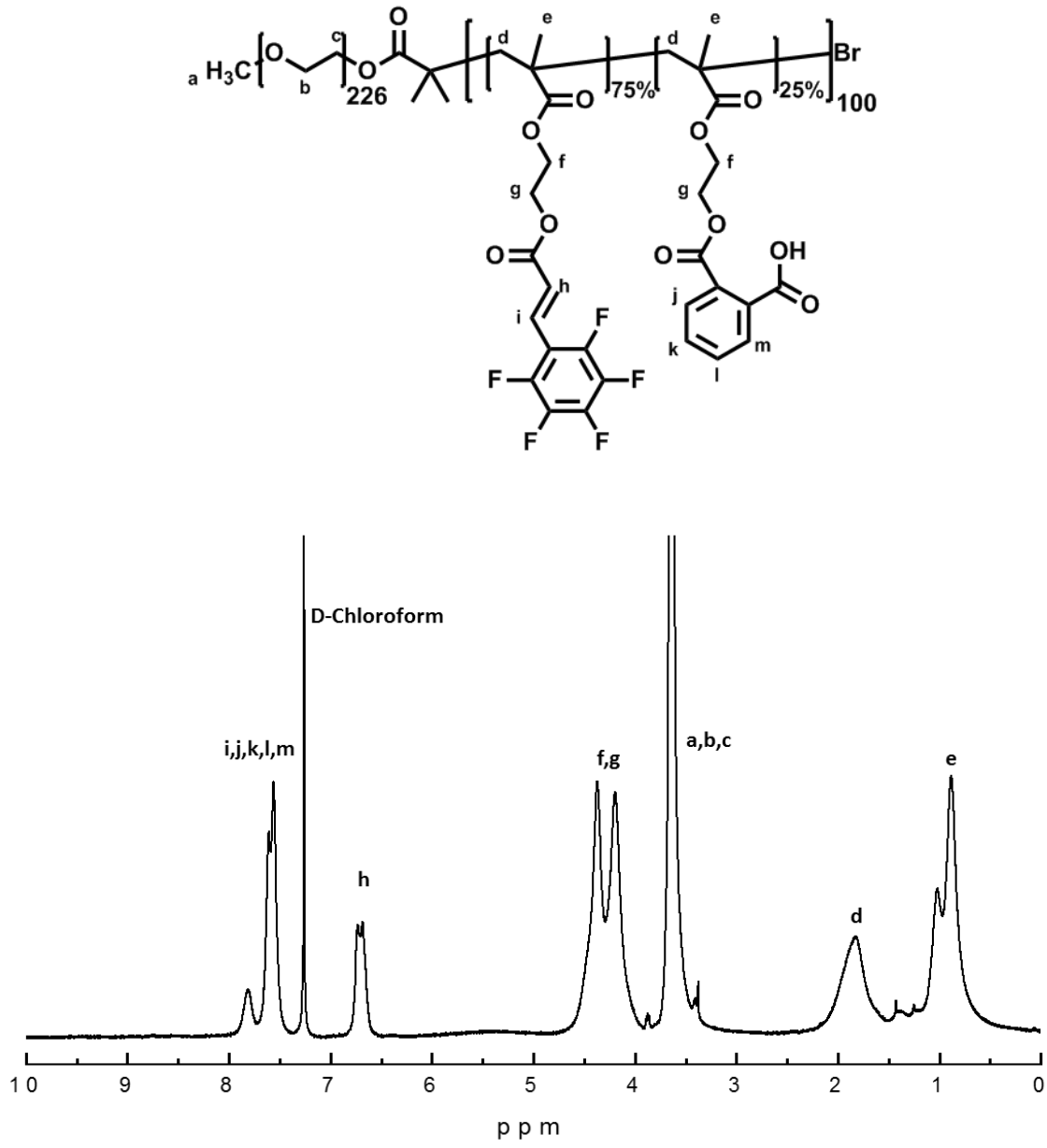

Figure 3-7. ^{1}H-NMR spectrum of PEO_{226}-*b*-P($FEMA_{75\%}$-*r*-$CA_{25\%}$)$_{100}$

The polymer PEO-*b*-P(FEMA-*r*-CA) was further characterized by SEC, and the results are shown below (Table 3-1 and Figure 3-8).

Table 3-1. Properties of the PEO-*b*-P(FEMA-*r*-PCA)

SEC	NMR			
M_n/M_w	*n*/*m*	*n*	*m*	*X*
1.16	2.26	226	100	0.75

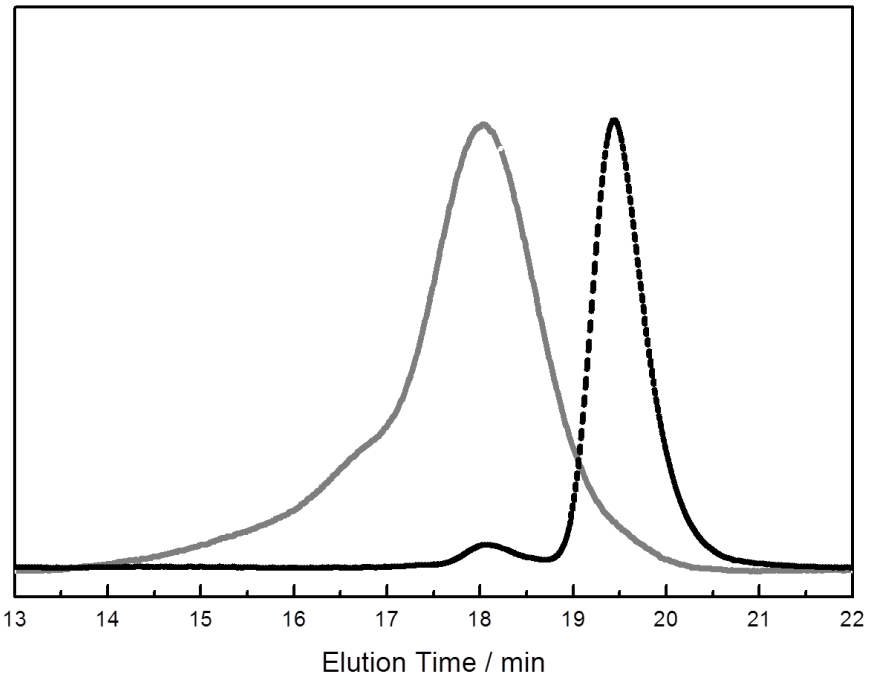

Figure 3-8. SEC traces of macroinitiator PEO-Br (dashed) and block copolymer PEO_{226}-*b*-P($FEMA_{75\%}$-*r*-$CA_{25\%}$)$_{100}$ (bold)

3.3 Preparation of the $_D$-ΦAA-Imprinted Polymer Nanospheres

The block copolymer PEO-*b*-P(FEMA-*r*-CA) was equilibrated overnight with the $_D$-ΦAA template in chloroform to undergo complexation with this template before it was subsequently dispersed as a micellar solution. The feed ratio of the carboxyl groups of PHEMA block to the $_D$-ΦAA template was 25:6.3. Because the template possessed a carboxyl group, the template could be anchored by electrostatic and hydrogen bonding interactions. In addition, the copolymer's pentafluorobenzene rings can also help anchor templates bearing aromatic rings.

As mentioned earlier, block copolymers can form micelles when they are dispersed into a block-selective solvent. In this case, we used chloroform/methanol (v/v = 0.5/9.5) as the solvent mixture for the copolymer dispersion. Chloroform is a good solvent for both of the two blocks of PEO-*b*-P(FEMA-*r*-CA), while methanol is a good solvent for the PEO block but a poor solvent for the P(FEMA-r-CA) block. When we slowly added the methanol into a chloroform solution of the copolymer and template, the block copolymer underwent self-assembly to form spherical micelles with the P(FEMA-*r*-CA) block aggregating as the core, and the PEO block stretching into the solution and forming the micellar corona. The bluish appearance of the solution provided visual evidence of the successful formation of micelles. To ensure that the template molecules were thoroughly wrapped within the polymer matrix of the core, the micellar solution was further equilibrated overnight prior to irradiation.

It is widely known that olefins with parallel orientation arrangement with a distance less than 0.42 nm can undergo [2+2] photodimerization when they are exposed to irradiation.[1] The FEMA double bond with its parallel orientation can also undergo a [2+2] photodimerization reaction when it is exposed to UV light.[2] In order to monitor the progress of this crosslinking reaction, the micellar solution was characterized by UV spectrophotometry. The FEMA block had an absorption peak ranging from 220 to 300 nm, and it exhibited its strongest absorbance at 260 nm. The decrease in the absorbance at 260 nm after the irradiation treatment indicated that the PFEMA block had become crosslinked. See Figure 3-9. Based on this decrease in the absorbance at 260 nm in the UV-vis spectrum, we calculated that FEMA exhibited a double bond conversion of 70% after 2 h of irradiation.

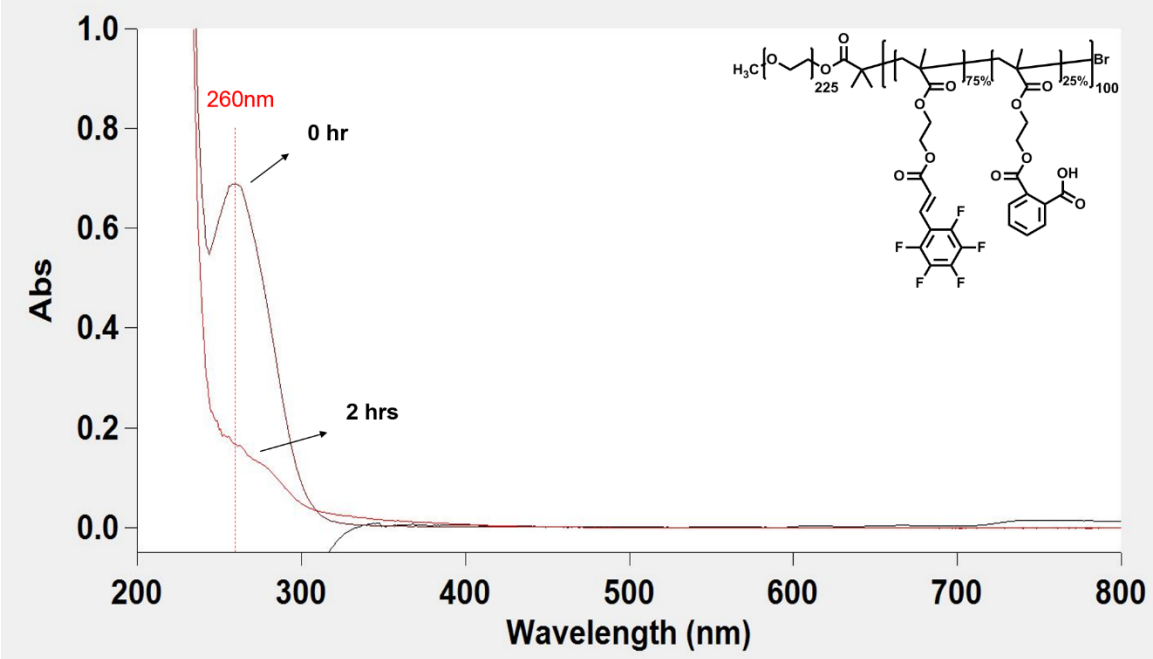

Figure 3-9. UV-vis spectrum of PEO-*b*-P(FEMA-*r*-CA) micellar solution after 0 and 2-hour irradiation.

The core of the micelle became structurally robust after it had been irradiated and became crosslinked. See Figure 3-10. The template was subsequently removed by dialysis against a chloroform/methanol mixture, thus leaving a polymer nanosphere with many hollow internal cavities left behind by the template molecules. In addition, these cavities had specific carboxyl group arrangements as well as a specific pentafluorobenzene ring arrangements and orientations that complemented the template. Due to the structural rigidity of these crosslinked spheres, these cavities remained intact after the removal of the template.

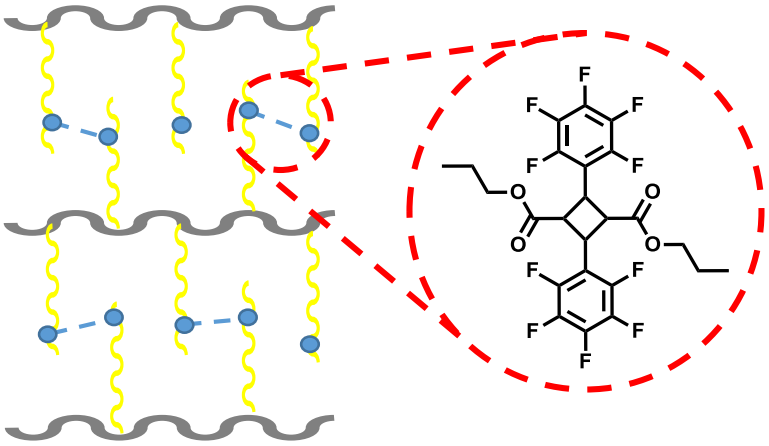

Figure 3-10. Schematic diagram of the interior structure of core of PEO-*b*-P(FEMA-*r*-CA) micelle.

The morphology of the micelle was characterized via atomic force microscopy (AFM) and dynamic light scattering (DLS). See Figure 3-11. As determined via AFM and DLS measurements, the average diameter of the micellar particles was 30.4 ±3 (n=20) and 52.5

nm, respectively. The polydispersity of the polymer nanospheres was measured to be 0.10 via DLS. See Table 3-2.

Dynamic light scattering can be used to determine the size distribution of a small particle in suspension. The diffusion coefficient D_h can be measured from instrument. Based on the Stokes–Einstein–Sutherland Equation [3-1], we can know the hydrodynamic diameter distribution of the spherical particles in suspension.

$$D_h = \frac{KT}{6\pi\eta r} \qquad [3\text{-}1]$$

Where, K denotes the Boltzmann's constant, T denotes the absolute temperature, η is the dynamic viscosity and r is the radius of the spherical particle.

Table 3-2. Hydrodynamic and Atomic Force Microscopic Diameters of PEO-*b*-P(FEMA-*r*-CA) micelle.

D_h/nm	K_2/K_1^2	D_A/nm
52.5	0.11	30.4 ± 3

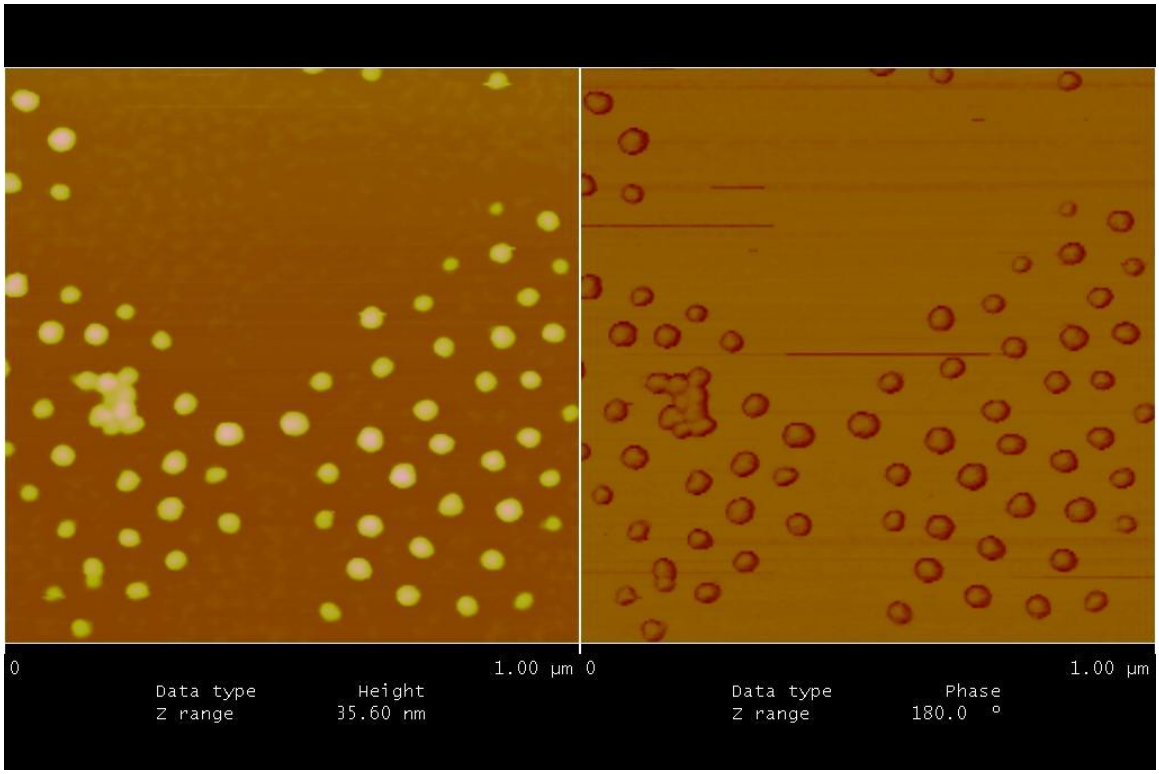

Figure 3-11. AFM image of the PEO-*b*-P(FEMA-*r*-CA) micelle on mica plate after irradiation.

3.4 Absorption Isotherms and Kinetics Obtained Using Phenylalanine Anilide as an Imprinting Template

PEO-*b*-P(FEMA-*r*-CA) nanospheres (10 mg) that had been imprinted with $_D$-ΦAA were dispersed into 1.0 mL of chloroform and the polymer nanosphere solution was placed into a dialysis tube with a M_w cut-off = 1,2000~1,4000 g/mol, which was subsequently immersed into a 9.0 mL chloroform solution containing a given amount of dissolved $_D$-

ΦAA or $_L$-ΦAA. The vial was sealed to prevent the chloroform from evaporating. The imprinted polymer nanospheres could not penetrate the membrane while the small template molecules from the surrounding solution could readily enter the dialysis tube without any resistance. The $_D$-ΦAA or $_L$-ΦAA molecules could thus be absorbed by the polymer nanospheres within the membrane tube, leading to a decrease in the $_D$-ΦAA or $_L$-ΦAA concentration in the surrounding chloroform solution. In addition, this absorption process could be conveniently monitored via UV-vis spectrophotometry. A given small amount of external chloroform solution was taken via a micro syringe and was transferred to a cuvette with a given amount of chloroform. The cuvette was then put in the UV-vis spectrophotometry for further characterization. The readings of absorbance at 240 nm with and without the polymer nanospheres were collected. According to the Equation [3-2], we were able to calculate the amount of the template molecules that had become absorbed by the polymer nanospheres based on the absorbance of the $_D$-ΦAA or $_L$-ΦAA in the presence and the absence of the $_D$-ΦAA-imprinted polymer nanospheres.

$$q = \frac{c_0 V_0}{m}\left(1 - \frac{R}{R_0}\right) \qquad [3\text{-}2]$$

Where q denotes the μmol of the template absorbed per gram of the polymer nanospheres. The terms c_0 and V_0 correspond to the initial concentration and the volume of template, respectively. Meanwhile, R and R_0 denote the absorbance of the template solution in the presence and the absence of the polymer nanospheres, respectively. In addition, m denotes

the mass of the P(FEMA-*r*-PCA) chains forming the core of the polymer nanospheres, which is also the mass of P(FEMA-*r*-CA) block.

The mechanism of the absorption process was also analyzed. Three types of molecular interactions were investigated here in the interior cavities between the copolymer's functional groups and template. These interactions included electrostatic interactions, hydrogen bonding and π-π stacking interactions between the benzene rings of *D,L*-ΦAA and pentafluorobenzene rings of PFEMA block. See Figure 3-12.

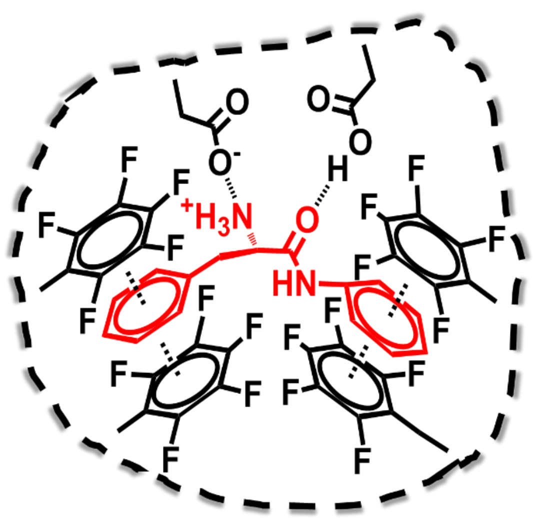

Figure 3-12. The schematic diagram of three types of molecular interactions between the polymer matrix and *D*-ΦAA molecule.

The *D*-ΦAA molecule possesses both an amino group ($-NH_2$) and a carbonyl group (-C=O). Meanwhile, the carboxyl groups of PEO-*b*-P(CEMA-*r*-CA) can participate in electrostatic

bonding interactions with the template's amino group as well as hydrogen bonding interactions with the carbonyl group. These two types of interactions can serve to anchor the $_D$-ΦAA molecules in the interior cavity in regular cases in the absence of the pentafluorobenzene ring. In the cases when PEO-*b*-P(FEMA-*r*-CA) was used as the imprinted polymer, in addition to electrostatic and hydrogen bonding interactions, there was also a third type of molecular interaction that could help retain the $_D$-ΦAA molecules, namely π-π stacking interactions.

As mentioned earlier, π-π stacking interactions were first discovered in 1960s. Many reports have demonstrated that fluorine-substituted aromatic rings have a lower electron density within their aromatic ring than is present among unsubstituted aromatic rings due to the presence of the fluorine substituents. Consequently, these fluorine-bearing aromatic rings have a greater tendency to behave as electron-acceptors in comparison with unsubstituted benzene rings, which are considered as electron-donors. It was also demonstrated that the interaction energies of π-π stacking interactions were affected by the nature of the substituent groups on the aromatic rings.[3]

Theoretically, $_D$-ΦAA molecule should only be absorbed by the appropriately imprinted bonding sites in the $_D$-ΦAA-imprinted polymer nanospheres. However, there are still some improperly imprinted bonding sites that may also absorb the $_D$-ΦAA molecules. These improperly imprinted bonding sites, which may not have the appropriate internal cavity shape or functional group arrangement, may be created during the preparation of the MIP.[4]

The reason why some $_L$-ΦAA may become absorbed by the polymer nanospheres is due to the existence of nonspecific binding sites.[4]

The kinetics of $_D$-ΦAA absorbed as a function of time from PEO_{226}-*b*-P($FEMA_{75\%}$-*r*-$CA_{25\%}$)$_{100}$ and PEO_{226}-*b*-P($CEMA_{75\%}$-*r*-$CA_{25\%}$)$_{100}$ is shown in Figure 3-13. The concentration of the external chloroform solution was 6.5 mM for both of the two types of polymer nanospheres. We can see from the curve that the $_D$-ΦAA sorption amount of PEO_{226}-*b*-P($FEMA_{75\%}$-*r*-$CA_{25\%}$)$_{100}$ and PEO_{226}-*b*-P($CEMA_{75\%}$-*r*-$CA_{25\%}$)$_{100}$ imprinted nanospheres increased quickly in the first 30 min and both reached plateau after 3.5 h. In this experiment, the maximum absorption amount calculated was around 226 ± 4 μmol/g for PEO_{226}-*b*-P($FEMA_{75\%}$-*r*-$CA_{25\%}$)$_{100}$ and 204 ± 4 μmol/g for PEO_{226}-*b*-P($CEMA_{75\%}$-*r*-$CA_{25\%}$)$_{100}$. We supposed that the reason why PEO_{226}-*b*-P($FEMA_{75\%}$-*r*-$CA_{25\%}$)$_{100}$ has a higher sorption amount than PEO_{226}-*b*-P($CEMA_{75\%}$-*r*-$CA_{25\%}$)$_{100}$ is because of the existence of π-π stacking interactions. With more possible binding sites, more cavities would be formed and more efficient cavities would be left during imprinting. The nanospheres prepared by PEO_{226}-*b*-P($FEMA_{75\%}$-*r*-$CA_{25\%}$)$_{100}$ thus has a better sorption capability.

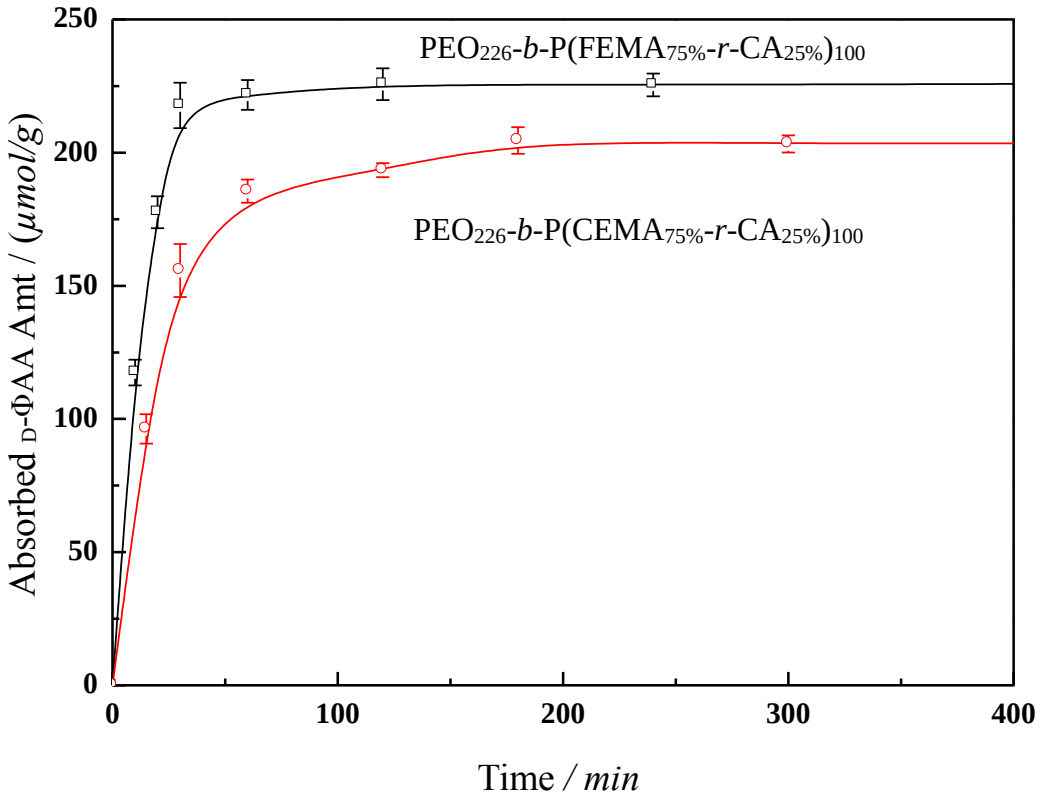

Figure 3-13. Variation of the amount of $_D$-ΦAA absorbed as a function of time from PEO$_{226}$-*b*-P(FEMA$_{75\%}$-*r*-CA$_{25\%}$)$_{100}$ and PEO$_{226}$-*b*-P(FEMA$_{75\%}$-*r*-CA$_{25\%}$)$_{100}$ imprinted nanospheres.

The ratio of the amount of $_D$-ΦAA absorbed relative to the amount of absorbed $_L$-ΦAA can reflect the selectivity of the imprinted polymer nanospheres for $_D$-ΦAA molecules. Based on our calculations, the maximum amount of $_D$-ΦAA absorbed by the PEO$_{226}$-*b*-P(FEMA$_{75\%}$-*r*-CA$_{25\%}$)$_{100}$ nanospheres was calculated as 248 ± 9 μmol/g, while the maximum amount of $_L$-ΦAA absorbed was 39.3 ± 0.3 μmol/g. See Figure 3-14, 3-15. Therefore, the imprinting factor (q_D/q_L) of the PEO$_{226}$-*b*-P(FEMA$_{75\%}$-*r*-CA$_{25\%}$)$_{100}$

nanospheres was 6.3 ± 0.2, which was even higher than the value reported previously by Liu and coworkers for their imprinted tadpoles.(a type of small MIPs prepared by single-chain block copolymer)[4] In comparison with other imprinted polymers that have utilized only one or two types of non-covalent interactions to anchor the template, the replacement of CEMA block with FEMA block to the binding system can introduce a third type of interaction in the polymer matrix for *D*-ΦAA, leading to a larger sorption capability for *D*-ΦAA. Besides, the introduction of covalent fluorine system can efficiently repel hydrocarbons and reduce the non-specific binding with *L*-ΦAA. With a higher sorption amount to *D*-ΦAA and a lower sorption amount to *L*-ΦAA, the imprinted polymer nanosphere thus has a higher imprinting factor than previously reported MIPs examples.[5,6] As reported by Moradian and coworkers, increasing the number of binding sites can also enhance the selectivity of MIP nanospheres.[7] See Table 3-3, 3-4.

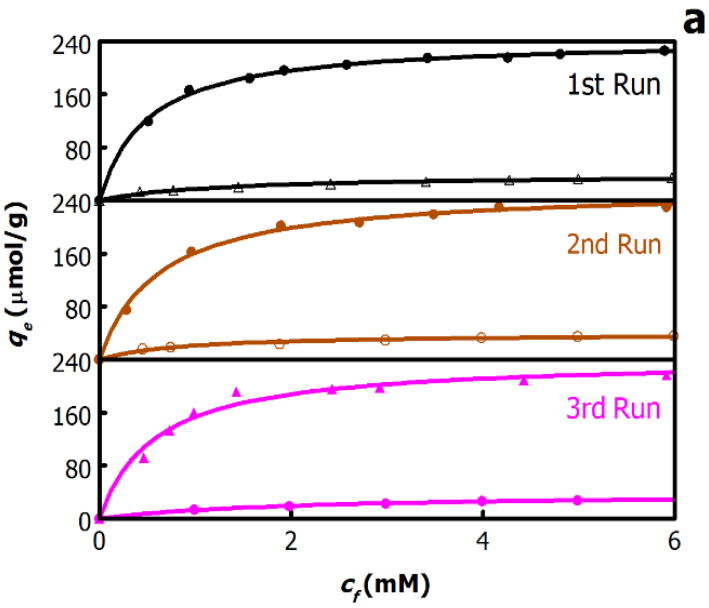

Figure 3-14. *D*-ΦAA and *L*-ΦAA sorption isotherm for PEO$_{226}$-*b*-P(FEMA$_{75\%}$-*r*-CA$_{25\%}$)$_{100}$ imprinted nanospheres.

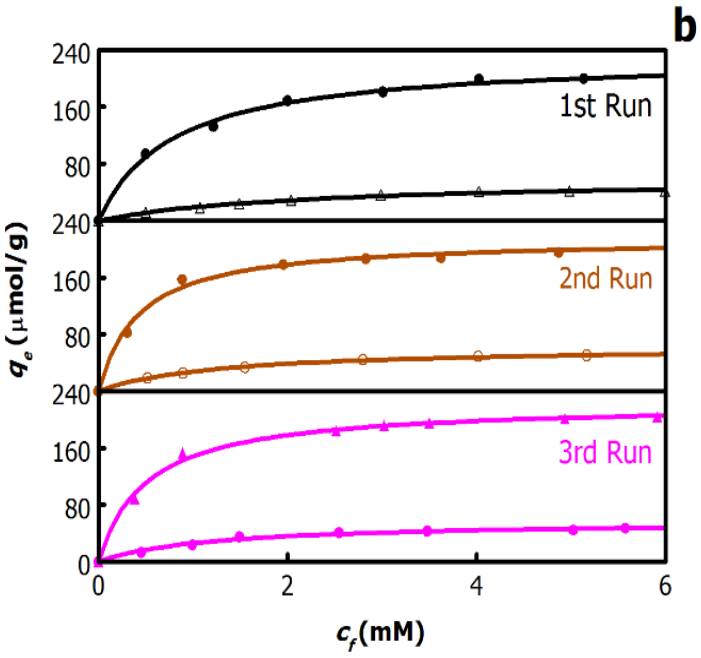

Figure 3-15. $_D$**-ΦAA and** $_L$**-ΦAA sorption isotherm for PEO$_{226}$-*b*-P(CEMA$_{75\%}$-*r*-CA$_{25\%}$)$_{100}$ imprinted nanospheres.**

Table 3-3. Results from treating the sorption data of using PEO$_{226}$-*b*-P(FEMA$_{75\%}$-*r*-CA$_{25\%}$)$_{100}$ as polymer and $_D$**-ΦAA as template.**

Run	q_D (μmol/g)	$10^{-3} \times K_D$ (M^{-1})	q_L(μmol/g)	$10^{-3} \times K_L$ (M^{-1})	q_D/q_L
1	244	2.03	39.4	0.81	6.2
2	259	1.63	39.5	1.14	6.6
3	242	1.73	39.0	0.49	6.2

Table 3-4. Results from treating the sorption data of using PEO_{226}-*b*-P($CEMA_{75\%}$-*r*-$CA_{25\%}$)$_{100}$ as polymer and $_D$-ΦAA as template.

Run	q_D (μmol/g)	$10^{-3} \times K_D$ (M^{-1})	q_L(μmol/g)	$10^{-3} \times K_L$ (M^{-1})	q_D/q_L
1	231	1.27	60	0.45	3.8
2	216	2.38	63	0.77	3.4
3	223	1.99	58	0.81	3.8

3.5 Imprinting Models.

According to previous studies, a wide range of binding constants have been observed among MIP systems. Assuming that all of the binding modes follow the Langmuir Model,[4] the data can be treated according to the Equation [3-3]:

$$q = \int_0^\infty \frac{Kc_f}{1+Kc_f}\, q(K)\, dK \qquad [3\text{-}3]$$

Where *K* denotes the binding constant and *q(K)* represents the binding capacity distribution function, which describes how the binding capacity *q* varies with the binding constant *K*.

In cases that lack sufficient data points, Equation [3-4] can be further abbreviated as:

$$q = \sum_i \frac{q_i K_i c_f}{1 + K_i c_f} \qquad [3\text{-}4]$$

The binding capacity and binding constant was evaluated by the Langmuir Equation [3-5] retaining only one binding constant:

$$\frac{c_f}{q_e} = \frac{c_f}{q_m} + \frac{1}{K q_m} \qquad [3\text{-}5]$$

Inserting all of the data, we can get the curve for each condition. See Figure 3-16, 17, 18, 19.

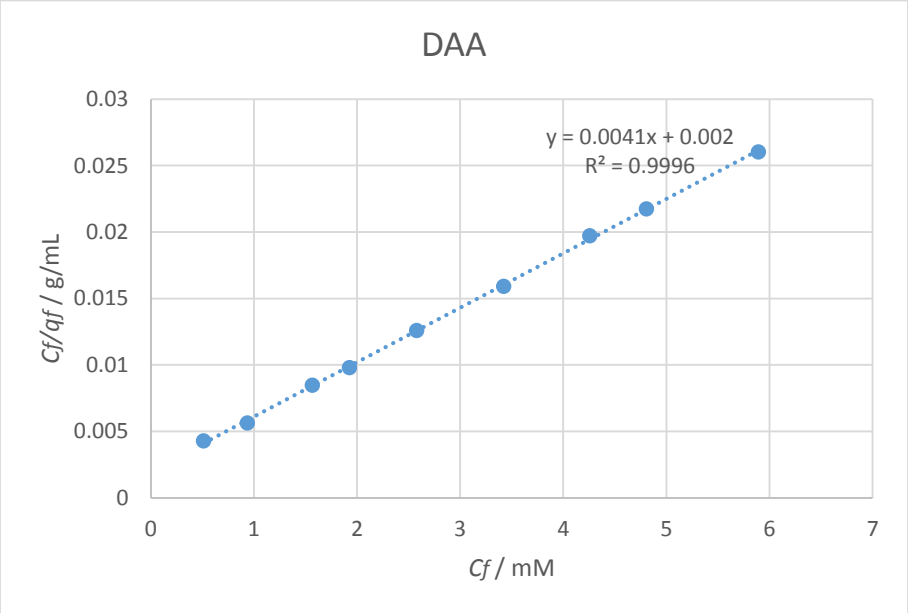

Figure 3-16. Isotherm data of PEO-b-P(FEMA-r-CA) nanospheres for D-ΦAA treated by Langmuir model (1st Run).

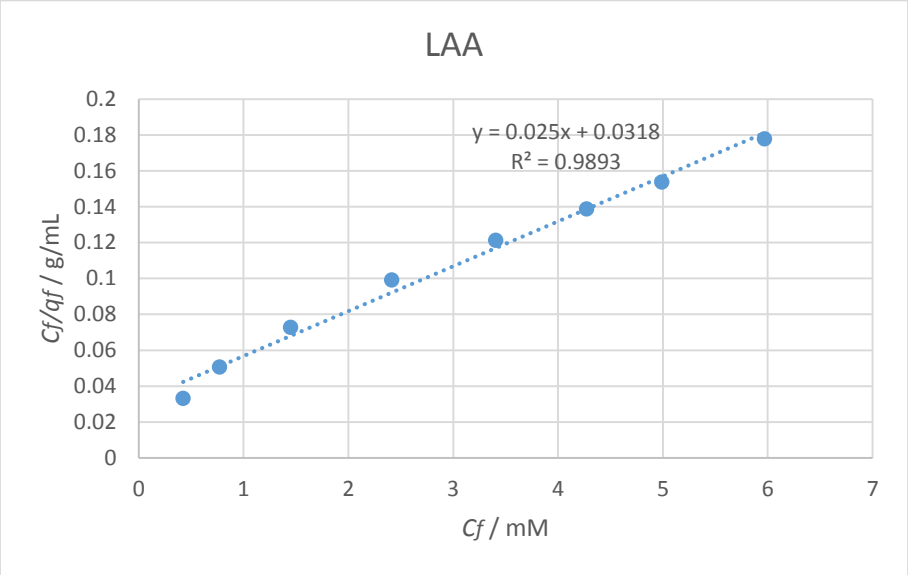

Figure 3-17. Isotherm data of PEO-*b*-P(FEMA-*r*-CA) nanospheres for $_L$-ΦAA treated by Langmuir model (1st Run).

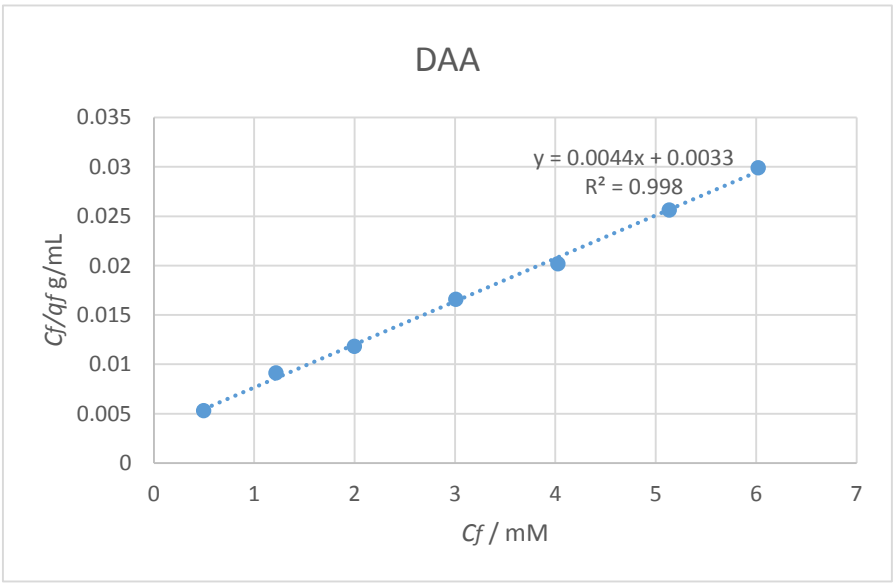

Figure 3-18. Isotherm data of PEO-b-P(CEMA-r-CA) nanospheres for $_D$-ΦAA treated by Langmuir model (1st Run).

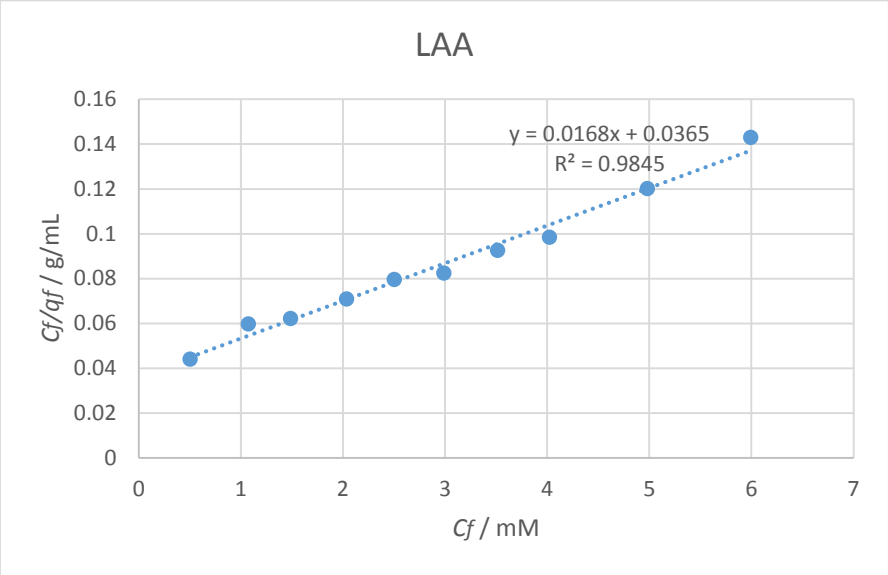

Figure 3-19. Isotherm data of PEO-*b*-P(CEMA-*r*-CA) nanospheres for $_L$-ΦAA treated by Langmuir model (1st Run).

We can obtain the maximum sorption amount and binding constant from the slope and intercept of the trendline, respectively. The R_v^2 values of the four curves were close to 1, demonstrating a good fit with the data. According to the four curves shown above, the maximum amount of $_D$-ΦAA absorbed by PEO-*b*-P(FEMA-*r*-CA) and PEO-*b*-P(CEMA-*r*-CA) was 248 ± 9 and 223 ± 8 μmol/g, respectively. Meanwhile, the maximum amount of $_L$-ΦAA absorbed by PEO-*b*-P(FEMA-*r*-CA) and PEO-*b*-P(CEMA-*r*-CA) was 39.3 ± 0.3 and 60.3 ± 2.5 μmol/g, respectively. The q_D/q_L value was 6.3 ± 0.2 for PEO-*b*-P(FEMA-*r*-CA), which is higher than the value of 3.7 ± 0.2 obtained for PEO-*b*-P(CEMA-*r*-CA). We attribute the enhanced selectivity exhibited by the PEO-*b*-P(FEMA-*r*-CA) nanospheres to the additional π-π stacking behavior.

3.6 Chapter Summary

This chapter we discussed the molecular structure and properties of PEO_{226}-*b*-P($FEMA_{75\%}$-*r*-$CA_{25\%}$)$_{100}$ using H-NMR spectroscopy and SEC. The results indicated that the PEO_{226}-*b*-$PHEMA_{100}$ was successfully synthesized via ATRP and the PEO_{226}-*b*-P($FEMA_{75\%}$-*r*-$CA_{25\%}$)$_{100}$ was obtained after successively reacted with pentafluorocinnamic acid chloride and phthalic anhydride. We further demonstrated that the FEMA units can be crosslinked after UV irradiation and can lock the core of the micelles.

The morphology and topology of micelles prepared by PEO_{226}-*b*-P($FEMA_{75\%}$-*r*-$CA_{25\%}$)$_{100}$ were studied using AFM and DLS. The AFM images showed that the crosslinked micelles were spherical and data collected from DLS revealed that the hydrodynamic diameter of the crosslinked micelles was 52.5 nm, with a polydispersity 0.10.

The sorption isotherms of $_D$-ΦAA and $_L$-ΦAA for imprinted polymer nanospheres were studied by UV-vis spectroscopy. A comparison was made between PEO_{226}-*b*-P($FEMA_{75\%}$-*r*-$CA_{25\%}$)$_{100}$ and PEO_{226}-*b*-P($CEMA_{75\%}$-*r*-$CA_{25\%}$)$_{100}$ based imprinted polymer nanospheres. The results indicated that the q_D/q_L value was 6.3 for PEO_{226}-*b*-P($FEMA_{75\%}$-*r*-$CA_{25\%}$)$_{100}$, which is higher than the value of 3.7 obtained from PEO_{226}-*b*-P($CEMA_{75\%}$-*r*-$CA_{25\%}$)$_{100}$. This finding suggested that the introduction of the pentabenzene ring in the system can help enhance the selectivity of polymer nanospheres for $_D$-ΦAA. Besides, as a result of a third type of molecular interactions, polymer nanospheres prepared from PEO_{226}-*b*-

P(FEMA$_{75\%}$-*r*-CA$_{25\%}$)$_{100}$ has a greater sorption capability than polymer nanospheres prepared from PEO$_{226}$-*b*-P(CEMA$_{75\%}$-*r*-CA$_{25\%}$)$_{100}$.

Reference

1. Bernstein, H. I.; Quimby, W. C. *J. Am. Chem. Soc*. **1943**, *63*, 1845-1846.
2. Yoriko Sonoda; *Molecules* **2011**, *16*, 119-148.
3. Dougal Cleland; Adam McCluskey *Org. Biomol. Chem.* **2013**, *11*, 4646-4656.
4. Gabriel Njikang; Guojun Liu; Liangzhi Hong *Langmuir* **2011**, *27*, 7176-7184.
5. Sellergren, B. *Makromol. Chem. Macromol. Chem. Phys* **1989**, *190*, 2703-2711.
6. Katz, A.; Davis, M. E. *Macromolecules* **1999**, *32*, 4113-4121.
7. Aydin Moradian; Klaus Mosbach *J. Mol. Recog*. **1989**, *4*, 167-169.

Chapter 4

Conclusion

4.1 Synthesis of PEO_{226}-*b*-$P(FEMA_{75\%}$-*r*-$CA_{25\%})_{100}$

The novel block copolymer PEO_{226}-*b*-$P(FEMA_{75\%}$-*r*-$CA_{25\%})_{100}$ was successfully synthesized as a part of investigation. Through the use of ATRP, we obtained PEO-*b*-PHEMA as the backbone. By reacting 2,3,4,5,6-pentafluorocinnamic acid with oxalyl chloride, we successfully synthesized 2,3,4,5,6-pentafluorocinnamic acid chloride with a high reaction activity. Treating the PEO-*b*-PHEMA with 2,3,4,5,6-pentafluorocinnamic acid chloride and phthalic anhydride subsequently yielded PEO_{226}-*b*-$P(FEMA_{75\%}$-*r*-$HEMA_{25\%})_{100}$ and PEO_{226}-*b*-$P(FEMA_{75\%}$-*r*-$CA_{25\%})_{100}$. The PFEMA block of PEO_{226}-*b*-$P(FEMA_{75\%}$-*r*-$CA_{25\%})_{100}$ was readily crosslinked under UV irradiation, thus forming a robust polymer matrix that provided an ideal candidate for molecular imprinting applications.

In this work, H-NMR spectroscopy and SEC were employed to study the molecular structure and polymer properties of the PEO_{226}-*b*-$P(FEMA_{75\%}$-*r*-$CA_{25\%})_{100}$. Even through the 2,3,4,5,6-pentafluorocinnamic acid chloride synthesized was directly used in next step without any characterization, it's safe to say that the chemical reaction and the acylation of PEO-*b*-PHEMA were successful by comparing the two H-NMR spectrums of PEO_{226}-*b*-$PHEMA_{100}$ and PEO_{226}-*b*-$P(FEMA_{75\%}$-*r*-$HEMA_{25\%})_{100}$.

4.2 Preparation of $_{D}$-ΦAA-Imprinted PEO_{226}-*b*-$P(FEMA_{75\%}$-*r*-$CA_{25\%})_{100}$ Nanospheres with a High Imprinting Factor.

Novel $_{D}$-ΦAA-imprinted PEO_{226}-*b*-$P(FEMA_{75\%}$-*r*-$CA_{25\%})_{100}$ nanospheres were prepared by following previously reported procedures.[4] The introduction of the PFEMA block can not only provide a robust core possessing interior imprinted cavities, but could also facilitate an additional non-covalent molecular interaction with the $_{D}$-ΦAA molecules via a π-π stacking interactions. This innovation can increase the selectivity of PEO_{226}-*b*-$P(FEMA_{75\%}$-*r*-$CA_{25\%})_{100}$ nanospheres for $_{D}$-ΦAA. In theoretical calculation, we employed the Langmuir model to analyze the sorption data. In comparison with the results obtained with imprinted nanospheres prepared from PEO_{226}-*b*-$P(CEMA_{75\%}$-*r*-$CA_{25\%})_{100}$, with a selectivity value towards $_{D}$-ΦAA as 3.7, the selectivity of PEO_{226}-*b*-$P(FEMA_{75\%}$-*r*-$CA_{25\%})_{100}$ nanospheres towards $_{D}$-ΦAA was much higher, reaching a value as high as 6.3.

In this work, DLS and AFM were employed to study the morphology and topology of PEO_{226}-*b*-$P(FEMA_{75\%}$-*r*-$CA_{25\%})_{100}$ micelles. By using AFM, we can know that the micelles are all spherical. With the help of DLS, we can know the hydrodynamic diameters and polydispersity of the micelles.

4.3 Significance of this Work

We reported the synthesis of novel block copolymer PEO_{226}-*b*-$P(FEMA_{75\%}$-*r*-$CA_{25\%})_{100}$ and a facile method for the preparation of MIP nanospheres with a high binding selectivity. The results of this investigation can provide valuable insight that may lead us in a new direction that utilizes PFEMA for the preparation of MIP particles. Also, because this polymer can be readily crosslinked when it is exposed to UV irradiation, PFEMA shows a strong potential as a precursor for the preparation of crosslinked materials. Moreover, with the introduction of a third type of binding mechanism, referring to π-π stacking interactions, $_D$-ΦAA-imprinted PEO_{226}-*b*-$P(FEMA_{75\%}$-*r*-$CA_{25\%})_{100}$ nanospheres showed improved selectivity over those bearing a PCEMA block as the imprinting matrix.

From the results we collected, the q_L/q_D value for polymer nanospheres prepared by PEO_{226}-*b*-$P(FEMA_{75\%}$-*r*-$CA_{25\%})_{100}$ was 6.3, which was 70% higher than the q_L/q_D value for polymer nanospheres prepared by PEO_{226}-*b*-$P(CEMA_{75\%}$-*r*-$CA_{25\%})_{100}$ and those traditional MIPs. Also, when templates containing phenyl rings are used, one can increase the selectivity by using monomers containing fluorinated phenyl rings, such as the fluorinated styrene.

4.4 Future work

In the future, further work will be needed to fully understand the mechanism of template sorption within this novel polymer matrix, particularly with respect to the newly introduced pentafluorobenzene moieties. Since the selectivity of the nanospheres has much relevance to the number of binding point, in order to clearly understand how the number of binding sites will affect the selectivity, templates with different numbers of benzene rings should be investigated to achieve a full demonstration.

In addition, we only applied Langmuir model to treat our data and haven't compare the curve fitting of the sorption isotherm with the one using other sorption models. Therefore, a systematic and mathematical study of different sorption models should be performed to determine which model provides the best accuracy in analyzing and calculating the amount of template absorbed as well as the binding constants between the templates and the PEO-*b*-P(FEMA-*r*-CA)-based MIP nanospheres.

What's more, besides the proper and nonproper sorption, the sorption amount caused by the non-specific binding sites should be taken into consideration. A serious of experiment should be prepared to examine the sorption amount caused by the non-specific binding between template and solid polymer nanospheres.

Appendix 1

Analysis of the floating behavior of a glass disk coated by a brand new fluorine-functionalized silica particle in a facile method

A1.1 Introduction

In recent years, people pay more attention to water strider for its interesting capability to walk on water freely instead of sinking into water.[1,2] Jiang et al reported [3] that water strider can walk effortlessly on water is due to the existence of hierarchical structure on their legs. Such a unique structure enables a superhydrophobic surface, which can repel water and support the standing of water strider. The hydrodynamic of water strider moving on water was then well explained, that it is the capillary force that is responsible for the standing and moving of floating objectives.[4]

Inspired by water strider, more bionic robots and devices have been invented.[5,6,7] However, compared to the lightweight water strider, dense objectives, such as cylindrical glass disk or spherical particles, usually has larger volume and higher density, making it difficult to for glass disk to float statically on the water surface as water strider. Besides, lacking of a hydrophobicity will also result in an easily wettable surface. Eventually, they will sink even though they bear way more upward buoyance force from water than water strider. In order to overcome this problem and design larger and denser new devices which can be applied

into aquatic mission, property modification must have to be done to the dense floating objectives to help increase their floating capability.

Two important factors affecting the water repellence of a material should be taken into consideration to address the problem: the chemical composition[8] of the materials and the topography of their surface.[9] A dense objective with a composition of elements with low surface energy, such as fluorine or a rough, hierarchical surface like the leg of water strider may be able to solve the floating issue. Hesla and Joseph analyzed the mechanism of the floating dense disk on water.[10] In their reports, they theoretically confirmed that if the target disk has enough superhydrophobicity, the water contact angle at the rim can somehow exceed 90 º, even if the vertical component of capillary force has already reached its maximal value. The feasibility of using dense objective as weight carrier was also reported by Joseph, who applied a Teflon-made cylindrical disk with low surface energy to investigate the fluid mechanism in a floating test. In their study, they observed that the maximal contact angle can actually be greater than 90 º.[11]

The other method to help improve the superhydrophobicity of a dense floating objective is to modify its surface. Compared to the modification of surface chemical composition, changing its topography is easier and more facile. One only has to coat the top surface with robust materials to form a rough layer with specific micro-structure, then such layer of coating can greatly increase the surface roughness and decrease the surface free energy.[12,13] Some crafts reported could perform a striking loading capacity without sinking.[5,14,15] Such

conclusions can not only help us with overcoming the floating issue of dense, large objectives, but also designing new aquatic devices with striking loading capacity.

In this study, we apply brand new fluorine-functionalized silica particles (FFSP) to coat the upper surface of a pristine glass disk to analyze its floating behavior in water. The maximal loading weight it can carry and the critical contact angle pinned to the rim was recorded. According to the results, the silica coated glass disk with a diameter of 2 inches showed a striking loading capacity. A critical contact angle higher than 110 ºwas observed, which is out of expect for a dense floating glass objective. Moreover, factors such as type of coating, coating thickness as well as the diameter of glass disk have also been investigated. All of these findings may provide guideness for designing new dense aquatic devices with superhydrophobicity in the future.

A1.2 Materials

Borosilicate glass disks were purchased from Chemglass. The diameters and thickness of disks used were 2 and 1.5 inches, 1.776 mm and 1.170 mm, respectively. Polystyrene (Mw=2000, 000 g/mol) was purchased from Aldrich Chemical Company, Inc. Trifluorotoluene (TFT) was purchased from ACROS. Tetrahydrofuran (THF) was purchased from Caledon Laboratory Ltd.

A1.3 Experimental Section

Coating materials used were fluorine-functionalized silica particles, PFOEMA and PS. The molecular structure of coated silica particles and PFOEMA (Mw=7000 g/mol) are showed in Figure A1-1.

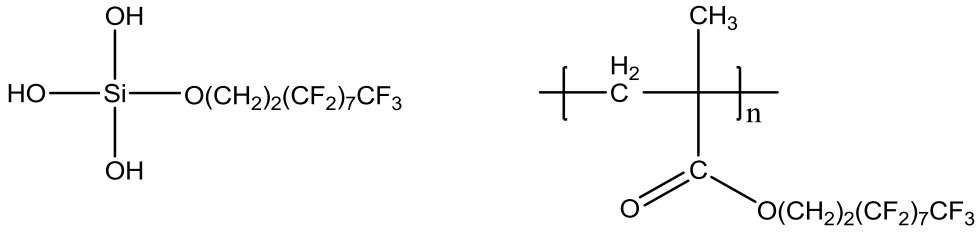

a **b**

Figure A1-1. Molecular structure of fluorine-functionalized silica particles (a) and Poly(2-(perfluorooctyl)ethyl methacrylate) (PFOEMA) (b)

A1.3.1 Preparation of bifunctionalized silica particle

Bifunctional silica particles were synthesized by a modified Stöber method.1 In a typical synthesis to produce 90 nm particles the following procedure was used. Initially, the solvent 9.0mL (absolute ethanol) was mixed with water 1.6mL (18 MΩ) and ammonia 2.5mL (2M in ethanol) and left to stir at 60ºC for 30mins. Then TEOS 2.2mL (~2.0g) was added to start the synthesis of the silica particles. The mixture was left to stir at 60ºC overnight. The functionalization agents were then added (typically 90uL of the F8 silane

and 7uL of C6 silane). The particles were recovered by centrifugation (3900RPM). The particles were then purified by redispersion in TFT (twice) or isopropanol (once) and then centrifugation (3900RPM).

A1.3.2 Preparation of coated glass silde

Three methods were applied here-spreading, spraying and spin coating to coat the borosilicate glass disks. For FFSP, a given amount of coated silica particle was dispersed in 1.0 ml TFT. After vibration and sonication for 1 min, the suspension was spread on the top surface of glass disk by dropping. After the evaporation of TFT, the FFSP-coated glass disk was further annealed in oven at 120 ℃ for 2 hrs before use. For PFOEMA, 30.0 mg of PFOEMA was dissolved in 1.0 ml THF. Then the polymer solution was spread on the top surface of glass disk by dropping. After the evaporation of THF, the PFOEMA-coated glass disk was further annealed in oven at 120 ℃ for 2hrs before use. For polystyrene, 30.0 mg of polystyrene was dissolved in 1.0 ml THF. The polymer solution was dropped on the top surface of glass disk and further cast by spin coating apparatus for 15 seconds. After the evaporation of THF, the polystyrene-coated glass disk was then put in oven and annealed under 120 ℃ for 2 hours.

A1.3.3 Set-up

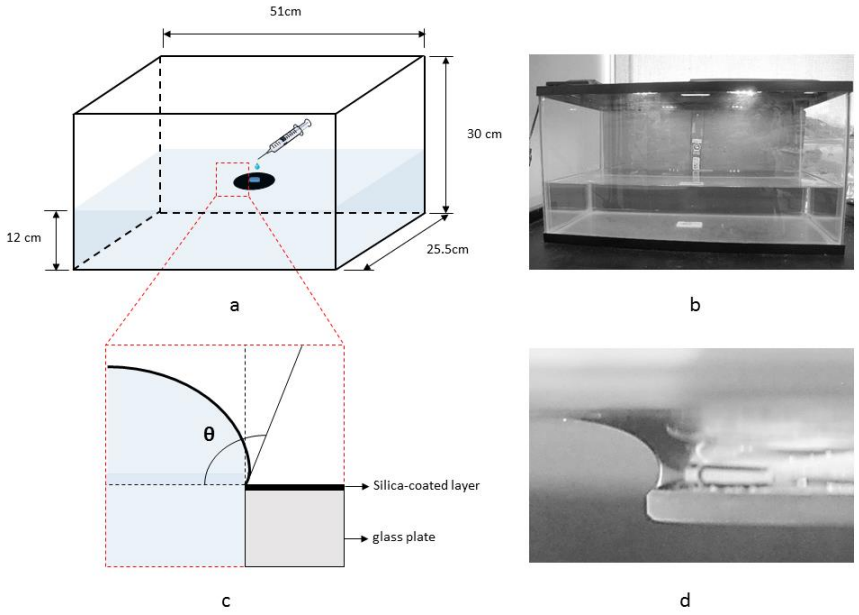

Figure A1-2. (a)(b)(c) Contact angle VS Loading mass measurement setup for a coated glass disk. (d) The meniscus formed around the FFSP coated (20.0 mg/ml) glass disk (*d* =2.0 inches) with a maximal loading mass (including the mass of glass disk and coating) 12.11 g and a maximal contact angle higher than 110 º.

The contact angle-loading mass relationship measurement was performed in a large, glass tank with length, width and height are 51 cm, 25.5 cm and 30 cm, respectively. A plastic cap of a vial was gently put on the centre of the glass disk. Water was added dropweise into the cap through a syringe. Mass of water was calculated based on the volume added. A digit camera (Canon PowerShot G11) was used to record the moment of meniscus with different loading mass.

A1.3.4 Instruments and Techniques

Scanning electron microscope (SEM) images of the glass samples were recorded using a FEI-MLA Quanta 650 FEG-ESEM instrument that was operated at 10-15 kV.

A1.4 Results and Dissusion

Mass of Borosilicate glass disks used here were 7.96 g and 2.86 g, with a density 2.21×10^3 kg/m^3 and 2.15×10^3 kg/m^3, respectively. The pristine glass disk (7.96 or 2.86 gram one) will sink instantaneously after put in water ($\rho=0.998\times10^3$ kg/m^3, 25 ℃). Instead, a glass disk with top side fully coated by hydrophobic coating can float on water. The other three sides of the glass disk were not coated, which can be wet by water. The immersing procedure (a-e) was illustrated in Figure A1-3.

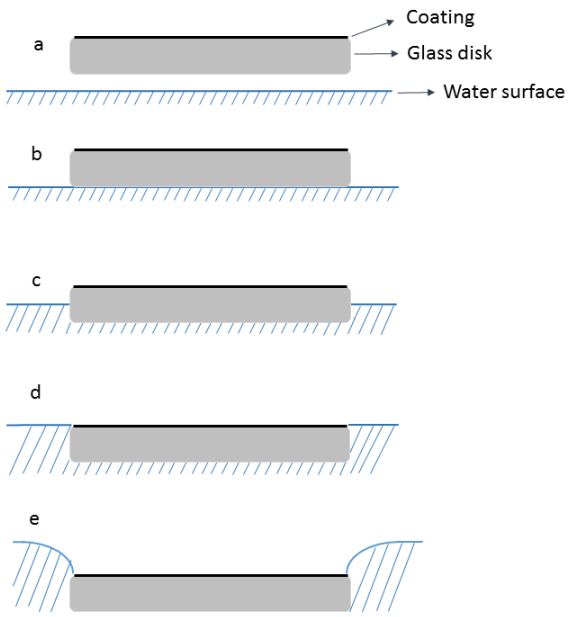

Figure A1-3

Figure A1-3. The immersing procedure of a coated glass disk

During the immersing of the coated glass disk, it will constantly underwent the upward pressure directly from water (Figure A1-3, c-e). After the glass disk completely sink into water, the water surface will start to deform (Figure A1-3, d). At this critical moment, due to the low wettability of surface-coated glass disk, water surface will instead form meniscus around the rim of glass slid (Figure A1-3, e). The formation of such meniscus was created by the surface tension, whose vertical component can help balance the gravity of glass disk together with the upward water pressure. In the vertical direction, four types of forces here contributed to the balance of the glass disk in the situation of "e" were investigated: the pressure from the water (F_1), the vertical component of water surface tension (F_2), the

gravity of water applied on the top of glass (F_3) and the gravity of glass disk (mg).See Equation [A1-1][A1-2][A1-3] below.

$$F_1 + F_2 = mg + F_3 \quad \text{[A1-1]}$$

$$F_1 = \rho g h \pi \alpha^2 \quad \text{[A1-2]}$$

Where ρ is the density of water, g is the gravity acceleration, h is the height from the horizontal water surface to the bottom side of glass disk and α is the radius of glass disk.

$$F_2 = 2\pi\alpha\gamma \sin \theta \quad \text{[A1-3]}$$

Where γ is the surface tension of water to air, θ is the contact angle.

Water pressure (F_1) is always proportional to height from horizontal water surface to the lower surface of glass disk. The capillary force is formed along the direction of tangent line between the meniscus curve and the upper surface of glass disk, with horizontal component $(2\pi\alpha\gamma \cos \theta)$ for wetting the surface and vertical component for supporting the floating objective. The upper surface of a pristine glass disk can be easily wetted by the horizontal component of the mensicus, leading to a sinkage. While the introduction of superhydrophobic coating can prevent the water from wetting the surface. The vertical

component of capillary force is proportional to the contact angle (CA) formed by the meniscus. When we start to add weight on the glass disk, both of the water pressure and vertical capillary force increased gradually before the CA reached 90 º. After the CA exceeded 90 º, the water pressure would continue increasing, while the vertical capillary force started to decrease. The instantaneously changing rate of water pressure (F_1') on height h, which is equal to $\rho g \pi \alpha^2$, is still higher than that of vertical capillary force (F_2'), which is mathematically equal to 0. The overall upward resultant of water pressure and capillary force will still continue increasing, making it possible for CA to exceed 90 ºand more loading, until the meniscus was not able to support the glass disk any more. The meniscus breaks along with the sinking of coated glass disk.

It is surprising to see that the maximal carrying mass added on FFSP coated glass disk (2 inches, coating concentration= 20 mg/ml) could up to be 4.13 gram, with a total mass 12.11g (7.96 g + 4.13 g + 0.02 g). The corresponding CA pinned at the rim was observed to be higher than 110 º(Figure A1-3, (d)). Figure A1-4 shows how the measured contact angles increase with increased loading weight when the fluorine-functionalized silica particle coated disks (c=20 mg/ml) were placed in a large tank. The maximal measured contact angles and loading weights for the two disks are given in table t1. It should be noted that the real maximal contact angle and loading weights are not given here because the meniscus would break before accurate measurements could be taken. Thus, the given values are slightly lower than the actual values.

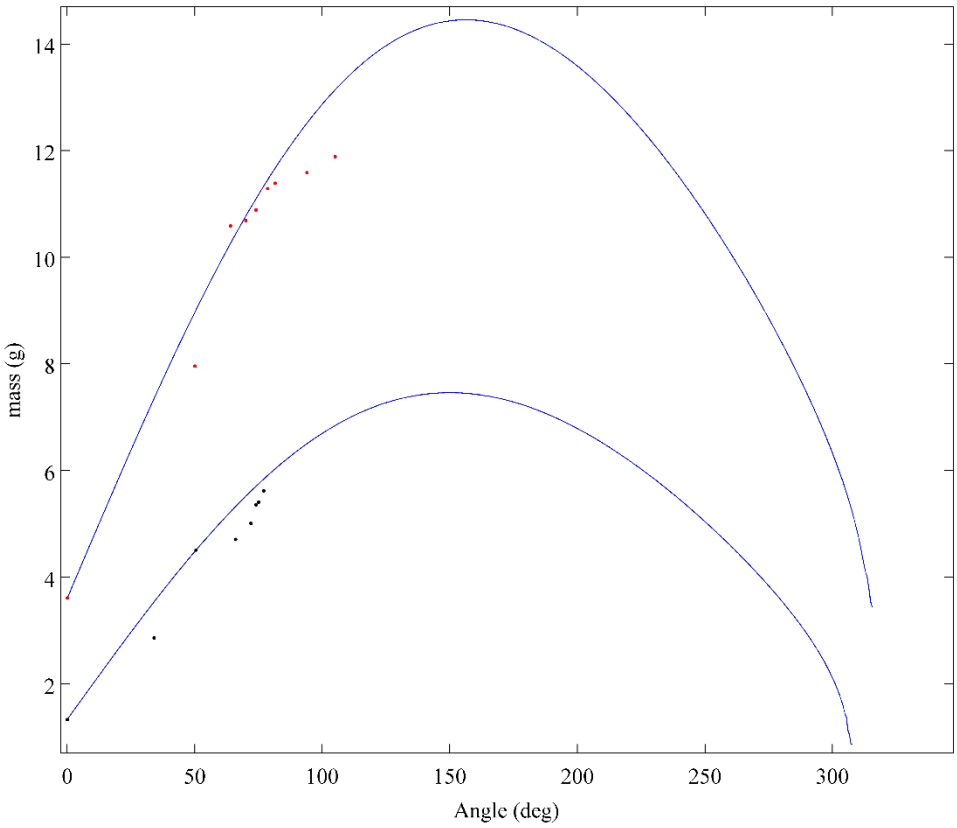

Figure A1-4. The relationship between contact angle and loading weight for silica-coated glass slides with a two inch diameter (red dots) and a 1.5 inch diameter (black dots). Theoretical fits are given in blue.

Table A1-1. Maximal measured contact angles and loading weights for the two disks.

Diameter of Disk (in)	Maximal Measured CA (θ)	Maximal Loading with the mass of glass disk(g)
1.5	>77	5.62
2	>110	12.11

The theoretical fits use the numerical method described by Hesla and Joseph.[11] Due to limited computational resources, a smaller mesh using 4000 points was used, instead of their 131 000 points. This reduces the accuracy of the given computational results but is accurate to within 1% of the results obtained by Helsa and Joseph. This method was chosen because it is able to describe contact angles greater than 90 °. Contact angles less than 90 ° degrees for floating cylinders have been observed experimentally and modeled theoretically.[10,16,17,18] The FFSP can greatly increase the surface hydrophobicity, making it as a striking loading carrier with a surface obtaining strong water repellence. To our best knowledge, this is the first time a contact angle greater than 110 °has been observed for a dense floating cylindrical glass disk.

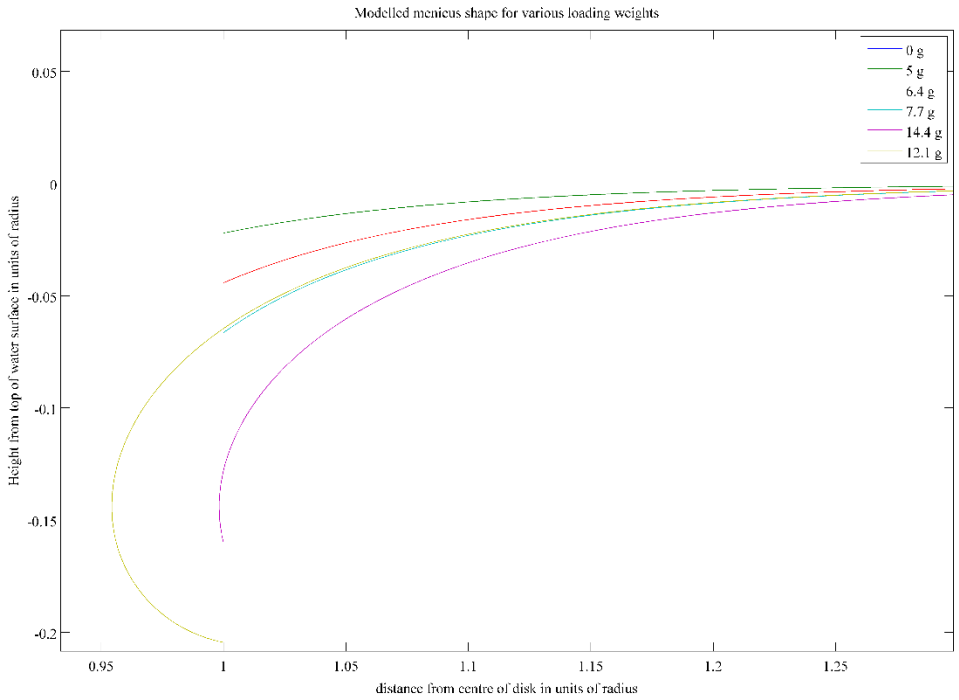

Figure A1-5. Theoretically generated meniscus shapes at different loading weights

Theoretically produced meniscus profiles were generated. Some examples are given in Figure A1-5. It can be seen that there can be multiple stable contact angles, as given by the Laplace equation, for a given loading weight. The yellow line, with a loading weight of 12.11 g (including the mass of coated glass disk), is less than the maximal loading weight, but has a higher contact angle than the maximal loading weight. This suggests that if meniscus never broke, there could be multiple stable configurations for a given loading weight. The more curved surfaces are much less stable and take more energy to produce, due to their larger surface area and greater surface depression. This is discussed in more detail below.

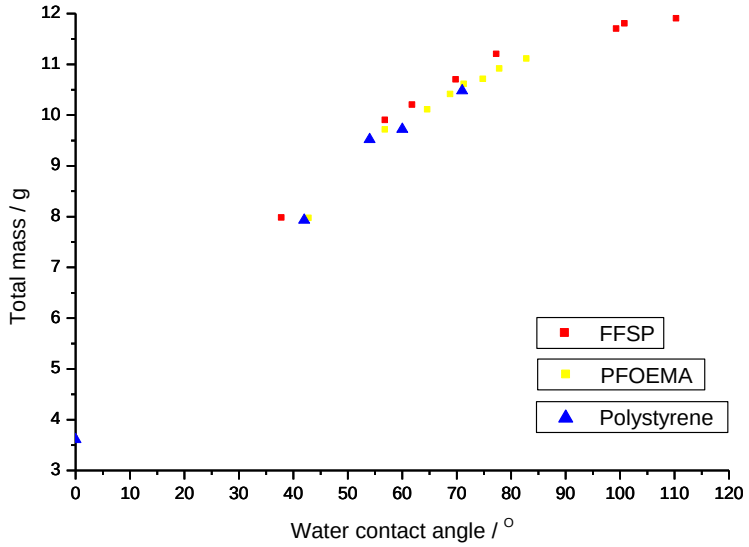

Figure A1-6. Relationships of water contact angle VS loading mass for a glass disk with different kinds of coatings.

Figure A1-6 shows the relationship between loading mass and three different coatings. FFSP is the most hydrophobic coating and polystyrene (PS) is the least hydrophobic among the three kinds of coating. At the interface, the system is governed by the Laplace Equation [A1-4] applied at interfaces.[20]

$$\Delta P = \gamma \left(\frac{1}{R_1} + \frac{1}{R_2} \right) = \rho g h \qquad \text{[A1-4]}$$

Here R_1 and R_2 are the principle radii of curvature of the surface, γ is the interfacial tension at the interface and ΔP is the pressure difference across the boundary, which is

equal to the liquid density, ρ, multiplied by gravitational acceleration, g, and the submerged depth of the disk, h. In this case, γ is given by the interfacial tension of water with air. Thus, each coating should obey this relation, no matter how hydrophobic its surface coating is. This is why they all follow the same relation between loading weight and contact angle.

Based on the data collected, it's interestingly to find that, no matter which kinds of coatings were used, the main portion of the two types of upward force (F_1 and F_2) was the pressure from water (F_1), which contributed almost 99% of the whole upward force, while the vertical component of surface tension (F_2) only contributed 1% to the whole upward force. When casted by the same coating with the same concentration, glass disk with a smaller diameter and submerging height will lead to a weaker upward water pressure ($F_1 \propto h\alpha^2$), which explains why coated glass disk with smaller diameter carried less mass.

Also seen in Figure A1-6 is that the more hydrophobic coatings allow for larger contact angles to be obtained. The main role of such superhydrophobic coating played here was to prevent the surface of glass disk from wetting and covering by the horizontal component of capillary force, making the formation of water meniscus become possible, which realizing the successful floatation of a glass disk . More mass could be added if the surface is more hydrophobic. It is also widely known that air trapped in between each silica particle at the contact point of water and surface can help increase the hydrophobicity as well.[19] Without such layer, glass surface can be could be easily wetted by water and a sinkage will

happen. Additionally, the larger contact angles create a higher energy surface due to the increase in surface area. This depressed surface also requires more energy to create due to the buoyancy created by depression.[18] The lower surface energy coating requires more energy to become wetted. Thus, a balance exists between these three energies: the wetting energy, the increase in surface area, and the buoyancy due to the deformed surface. A greater understanding of how the surface breaks needs to be obtained, through video or still shots, in order to properly evaluate these energy terms. One needs to understand how the surface changes at the moment the meniscus breaks and how the surface is wet.

Then we applied different concentration of FFSP suspension to coat the glass disk to study its effect on maximal loading capacity of glass disk. See Figure A1-7. We found that even through the concentration of FFSP increases from 10 mg/ml to 45 mg/ml, the maximal loading weight turned out to be very close. This study was performed on the regular microscope glass slide and the water contact angle of glass disks with different coating concentration were investigated. For a pristine glass disk, a droplet will easily spread on its surface, resulting in the contact angle mathematically equal to 0. When the concentration of FFSP coating increase, the corresponding contact angle will increase as well. When the FFSP concentration reached a critical value, water contact angle will stop increasing and remain constant. The result showed that the water contact angles after critical FFSP concentration were very close (157~159 °).

Assuming that there is no silica aggregation and all of the silica particles are well and uniformly arrange on the glass surface, the average thickness of a subsingle-layer (a) and a uniform single-layer (b) coated silica is 90.0 nm (c≈0.28mg/ml), see Figure A1-8, which is equal to the diameter of a silica particle purchased. Theoretically, water droplet might wet the subsingle-layer one while will stand on the single-layer one. However, water droplet can somehow wet the surface (CA<40^{o}) in both of these two conditions. This may be because in real situation, silica particles will aggregate to some extent. Some areas of glass disk may not be coated and thus can be wet by water. Under these concentrations, the glass surface was not able to support floatation. When the coating thickness increase from 90.0 nm (c≈ 0.28 mg/ml) to 2.04 μm (c≈ 6.94 mg/ml), the fluorine-functionalized silica particles will gradually pack layer by layer. The surface of glass slide will be uniformly and nicely covered and water contact angle starts to increase correspondingly from 33 ℃to 158°. When the coating thickness is higher than 2.04 μm (c≈ 6.94 mg/ml), water contact angle reaches its maximal value and become stable. Under such concentrations (c≥ 6.94 mg/ml), the FFSP coating enable the floatation of a glass slide.

We can see from the Figure A1-7, 2.04 μm (c≈ 6.94 mg/ml) is the critical thickness below which coating thickness can affect the surface free energy of FFSP coating. As seen in Figure A1-10, the thicker coatings have showed a uniform arrangement. As a result of densely packed, multiple-layer coatings with a thickness higher than or equal to 2.04 μm share the similar surface roughness and surface energy, which can explain why the water contact angles and the maximal loading mass were pretty similar.

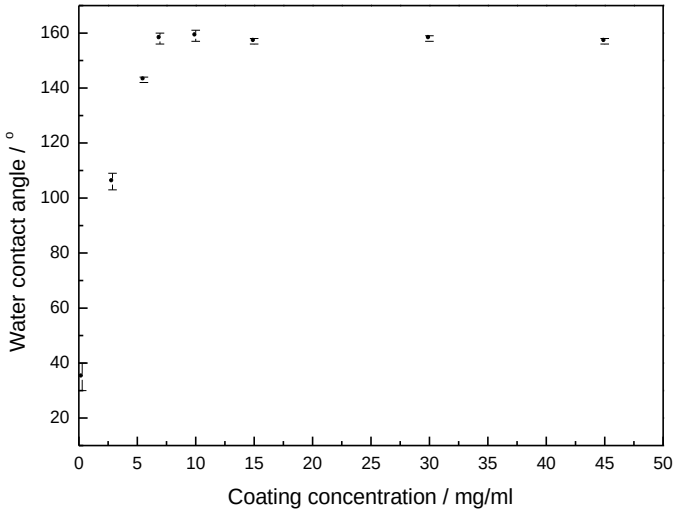

Figure A1-7. Relationship between coating concentration (mg/ml) and water contact angle ( ).

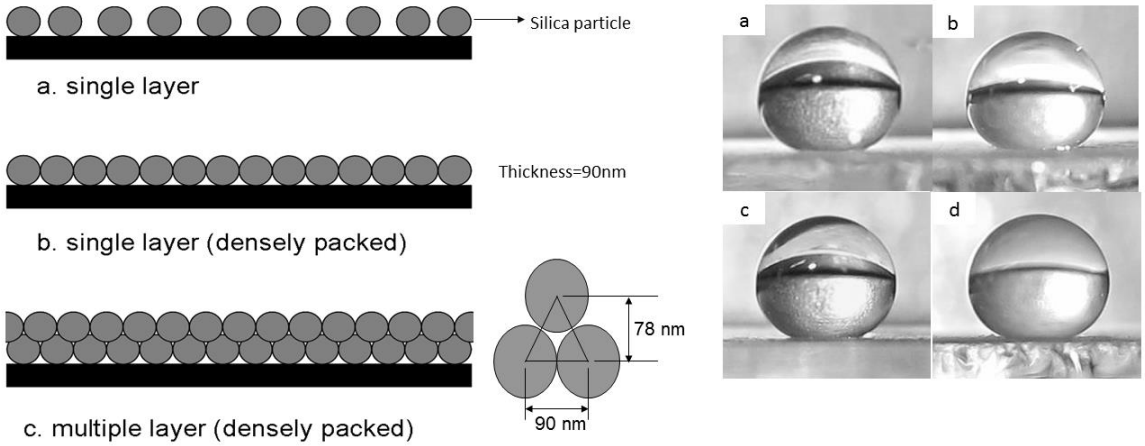

Figure A1-8. (A) Illustration for plate with single layer, single layer (fully coated) and

multiple layers. (B) Images of water droplet on coated glass slide with different coating concentration: 10mg/ml, 15mg/ml, 30mg/ml and 45mg/ml.

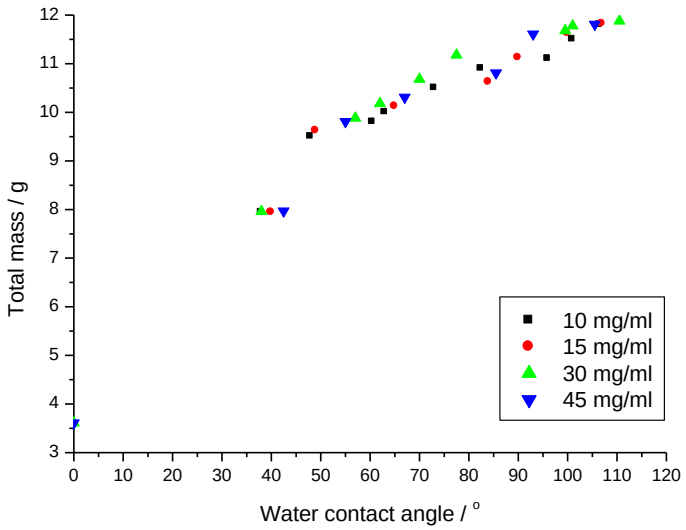

Figure A1-9. Relationship between contact angle and loading weight for coated glass slide with different coating concentration.

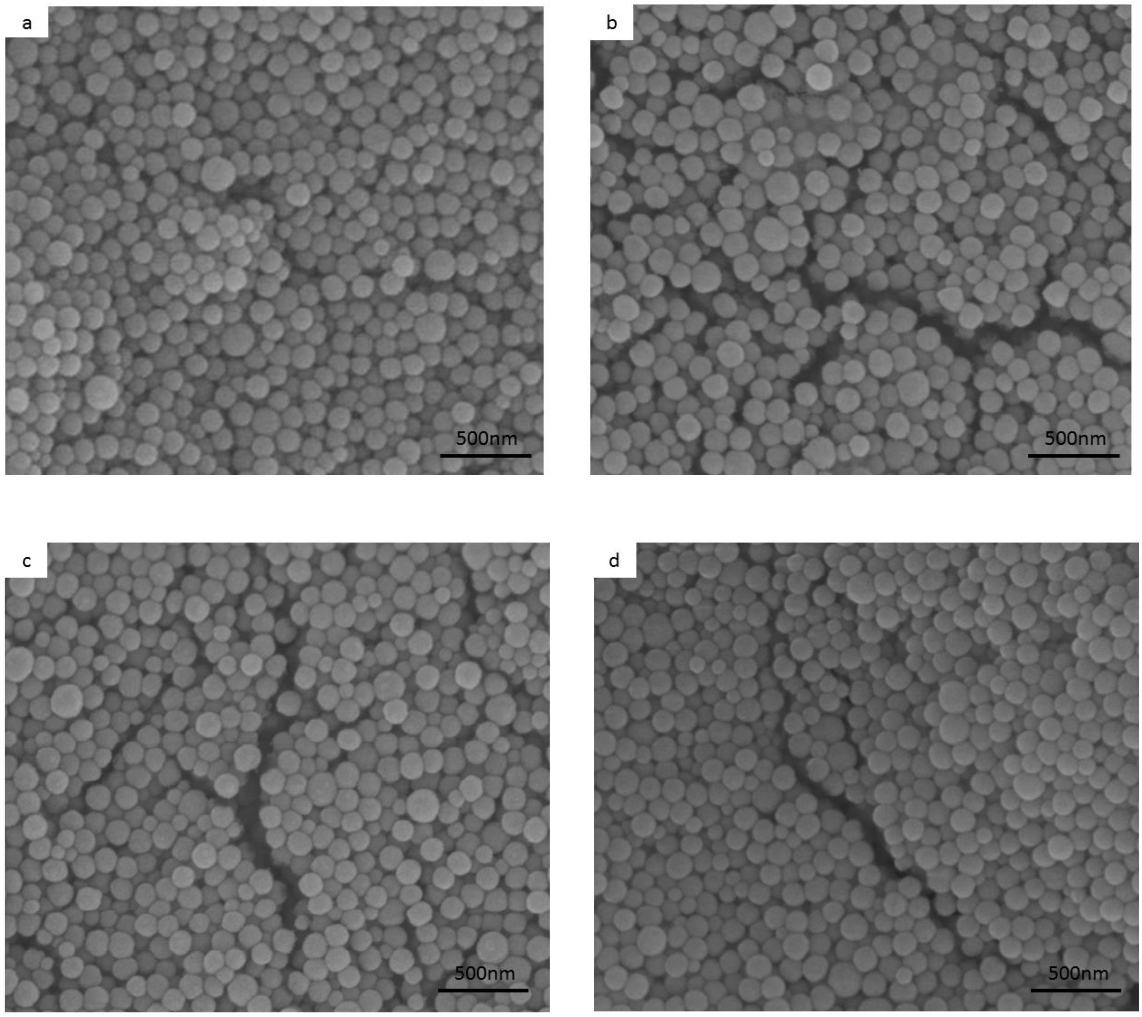

Figure A1-10. SEM images of silica particles on glass slide with different coating concentration. (a) 10mg/ml, (b) 15mg/ml, (c) 30mg/ml and (d) 45mg/ml.

A1.5 Conclusion

In summary, we have examined the feasibility of applying a dense glass disk coated by hydrophobic coatings in loading mass. The fluorine-functionalized silica particles coated glass disk turned out to acquire a carry capability of 12.11 gram. A striking maximal contact angle higher than 110 ^{o}was also observed. Moreover, factors affecting the maximal carrying capacity was also analyzed. It is believed that the smaller the diameter, the lighter mass it can carry. Also, we demonstrated that the maximal loading capacity has much relevance to the kinds of hydrophobicity of coatings. Fluorinated-silica particle coatings performed better carry capacity than PFOEMA and polystyrene, for the reason that fluorinated-silica particle coatings contains not only fluorine groups, whose surface energy is the lowest among all of the elements; but also can form bumpy surface, which can further enhance the non-wettability. It is also confirmed that the coating thickness of fluorine functionalized silica particles will affect the floating capability. Only if the coating concentration is equal to or higher than the 6.94 mg/ml, it is possible for the glass disk to float on water. The great superhydrophobicity of such fluorinated-functionalized silica particles can be applied as industrial coating. We expect our present studies can further guide the design and application of dense aquatic device and micro-robotic with superhydrophobicity in a facile way.

Reference

1. Dickinson, M., Animal locomotion: How to walk on water. *Nature* **2003,** *424* (6949), 621-622.
2. Denny, M. W., Paradox lost: answers and questions about walking on water. *J. Exp. Biol.* **2004,** *207* (10), 1601-1606.
3. Gao, X. F.; Jiang, L., Water-repellent legs of water striders. *Nature* **2004,** *432* (7013), 36-36.
4. Bush, J. W. M.; Hu, D. L., Walking on water: Biolocomotion at the interface. In *Annual Review of Fluid Mechanics*, Annual Reviews: Palo Alto, 2006; Vol. 38, pp 339-369.
5. Zhang, X. B.; Zhao, J.; Zhu, Q.; Chen, N.; Zhang, M. W.; Pan, Q. M., Bioinspired Aquatic Microrobot Capable of Walking on Water Surface Like a Water Strider. *ACS Appl. Mater. Interfaces* **2011,** *3* (7), 2630-2636.
6. Song, Y. S.; Sitti, M.; Ieee, STRIDE: A highly maneuverable and non-tethered water strider robot. In *Proceedings of the 2007 Ieee International Conference on Robotics and Automation, Vols 1-10*, Ieee: New York, 2007; pp 980-984.
7. Song, Y. S.; Sitti, M., Surface-tension-driven biologically inspired water strider robots: Theory and experiments. *IEEE Trans. Robot.* **2007,** *23* (3), 578-589.
8. Woodward, J. T.; Gwin, H.; Schwartz, D. K., Contact angles on surfaces with mesoscopic chemical heterogeneity. *Langmuir* **2000,** *16* (6), 2957-2961.
9. Sun, T. L.; Feng, L.; Gao, X. F.; Jiang, L., Bioinspired surfaces with special wettability. *Accounts Chem. Res.* **2005,** *38* (8), 644-652.
10. Hesla, T. I.; Joseph, D. D., The maximum contact angle at the rim of a heavy floating disk. *J. Colloid Interface Sci.* **2004,** *279* (1), 186-191.
11. Singh, P.; Joseph, D. D., Fluid dynamics of floating particles. *J. Fluid Mech.* **2005,** *530*, 31-80.
12. Shibuichi, S.; Onda, T.; Satoh, N.; Tsujii, K., Super water-repellent surfaces resulting from fractal structure. *J. Phys. Chem.* **1996,** *100* (50), 19512-19517.
13. Onda, T.; Shibuichi, S.; Satoh, N.; Tsujii, K., Super-water-repellent fractal surfaces. *Langmuir* **1996,** *12* (9), 2125-2127.
14. Jin, H.; Kettunen, M.; Laiho, A.; Pynnonen, H.; Paltakari, J.; Marmur, A.; Ikkala, O.; Ras, R. H. A., Superhydrophobic and Superoleophobic Nanocellulose Aerogel Membranes as Bioinspired Cargo Carriers on Water and Oil. *Langmuir* **2011,** *27* (5), 1930-1934.
15. Pan, Q. M.; Wang, M., Miniature Boats with Striking Loading Capacity Fabricated from Superhydrophobic Copper Meshes. *ACS Appl. Mater. Interfaces* **2009,** *1* (2), 420-423.
16. Mao, Z. S.; Yang, C.; Chen, J. Y., Mathematical modeling of a hydrophilic cylinder floating on water. *J. Colloid Interface Sci.* **2012,** *377*, 463-468.
17. Extrand, C. W.; Moon, S. I., Will It Float? Using Cylindrical Disks and Rods to Measure and Model Capillary Forces. *Langmuir* **2009,** *25* (5), 2865-2868.
18. Chang, F. M.; Sheng, Y. J.; Tsao, H. K., Superhydrophobic floatability of a hydrophilic object driven by edge effect. *Appl. Phys. Lett.* **2009,** *95* (20), 3.

19. Zimmermann, J.; Reifler, F. A.; Fortunato, G.; Gerhardt, L. C.; Seeger, S., A Simple, One-Step Approach to Durable and Robust Superhydrophobic Textiles. *Adv. Funct. Mater*. **2008,** *18* (22), 3662-3669.
20. Princen, H. M. In *Surface and Colloid Science* Vol. 2; Matijevic, E., Ed.; Wiley - *Interscience*, **1969**, 1–5.